

**Microdosimetric Evaluation of Photon Emitting Brachytherapy Sources in Tissue-Specific  
Models**

Joseph M. DeCunha

Master of Science

Medical Physics Unit

McGill University

Montreal, Quebec

2020-08-30

A thesis submitted to McGill University in partial fulfillment of the requirements of the degree  
of Master of Science in Medical Physics

©Joseph DeCunha 2020

## Acknowledgements

I would like to acknowledge the harmful myth of meritocracy in the North American context. As a white settler on unceded and occupied lands I have benefitted from innumerable privileges afforded to me by a fundamentally unjust society. All settlers and I benefit from affluence and safety that are the direct result of ongoing exploitation of racialized peoples and indigenous lands. Some tangible manifestations of that prosperity include access to a remarkable and well-funded public education system and a publicly funded healthcare system, without which this work would not have been possible. In addition to my settler privilege my gender identity has allowed me to pursue an education in the sciences free from harassment, ostracization, or isolation. I have benefitted from a lifetime of unreciprocated emotional labour and material assistance from women. My journey in medical physics began because of the remarkable trust of Dr. Shirin Enger. Dr. Enger has allowed me to work on ambitious projects, provided me with resources, support, and granted me opportunities it is hard to imagine any other supervisor allowing me so early in my career.

I am extremely grateful for the advice and technical knowledge I have received from conversations with individuals including Dr. Fernanda Villegas, Dr. Ives Levesque, Gabriel Famulari, Tristan Shoemaker, Maclean Rouble, Peter Kim, Anastasia Kolokotronis, Soud Kharusi, and so many others. This work was conducted within McGill's Medical Physics Unit, which could not exist without the extraordinary work of Dr. Jan Seuntjens and Margery Knewstubb.

This work was supported by the Natural Sciences and Engineering Research Council of Canada (grant number 241018), Collaborative Health Research Projects (grant number 523394-18), and the Fonds de recherche du Québec – Santé (file number 277159).

## Abstract

The biological effects of ionizing radiation depend on the tissue, tumor type, radiation quality, and patient-specific factors. Inter-patient variation in cell/nucleus size may influence patient-specific dose response. However, this variability in dose response is not well investigated due to a lack of available cell and nucleus size information. Microscopic energy deposition distributions from ionizing radiation are used to predict biological effects of an irradiation and vary depending on biological target size.

In this thesis methods to derive cell/nucleus size distributions from digital images of 2D histopathological samples are presented. 3D digital tissue models containing volumes with equivalent cell spacing, nucleus radius, and packing density to cancerous tissues are developed. Microdosimetric distributions of lineal energy for photon emitting brachytherapy sources are then determined in the cancerous nuclei of patient-specific models. Fast methods for the determination of microdosimetric distributions are developed using a summation technique, which allows for the calculation of patient-specific microdosimetric distributions in seconds with a desktop computer.

A dependence of microdosimetric distributions on target spacing is observed which has not been reported elsewhere and requires further investigation. The tissue-specific models developed in this thesis have applications in radiopharmaceutical therapy, conventional radiation therapy, and basic science. With appropriate biological inputs the microdosimetric distributions computed in this thesis can yield a patient-specific relative biological effectiveness as part of a multiscale treatment planning approach.

## Résumé

Les effets biologiques des rayonnements ionisants dépendent du tissu, du type de tumeur, de la qualité du rayonnement et des facteurs spécifiques au patient. Les variations de la taille des cellules / noyaux peuvent influencer la réponse d'un patient spécifique à la dose. Cependant, cette variabilité de la réponse à la dose n'est pas bien étudiée en raison du manque de données disponibles sur la variation de la taille des cellules / noyaux. Les distributions microscopiques des dépôts d'énergie provenant des radiations ionisantes sont utilisées pour prédire les effets biologiques d'une irradiation et varient en fonction de la taille de la cible biologique.

Dans cette thèse, sont présentées des méthodes pour dériver des distributions de taille de cellules / noyaux à partir d'images numériques d'échantillons histopathologiques 2D. Des modèles de tissu numériques 3D, contenant des volumes avec un espacement cellulaire, un rayon de noyau et une densité de remplissage équivalents aux tissus cancéreux, sont développés. Les distributions microdosimétriques d'énergie linéaire pour les sources de curiethérapie émettant des photons sont ensuite déterminées dans un modèle des noyaux cancéreux spécifique au patient. Des méthodes rapides pour la détermination des distributions microdosimétriques sont développées en utilisant une technique de sommation, qui permet le calcul des distributions microdosimétriques spécifiques au patient en quelques secondes avec un ordinateur de bureau.

Une dépendance des distributions microdosimétriques en fonction de l'espacement des cibles est observée, ce qui n'a pas été rapporté ailleurs et qui nécessite des recherches plus approfondies. Les modèles spécifiques aux tissus développés dans cette thèse ont des applications dans la thérapie radiopharmaceutique, la radiothérapie conventionnelle et la science fondamentale. Avec des données biologiques appropriées, les distributions microdosimétriques calculées dans cette thèse

peuvent donner une efficacité biologique relative spécifique à un patient, dans le cadre d'une approche de planification de traitement "multiscale".

## **Preface and Contribution of Authors**

Chapters 2 and 3 of this thesis are lightly modified from two manuscripts which are intended to be submitted for peer review. In order to allow each section of the thesis to be understood independently acronyms are redefined in each chapter. Key concepts present in the introductory chapter of the thesis are reintroduced in Chapters 2 and 3. The intended title and authors list of the manuscripts are respectively as follows:

### **Development of Patient-Specific 3D Models from Histopathological Samples for Investigations in Radiation Therapy**

Joseph M. DeCunha, Christopher M. Poole, Martin Vallières, Jose Torres, Sophie Camilleri-Broët, Roni F. Rayes, Jonathan D. Spicer, Shirin A. Enger

and

### **Patient-Specific Microdosimetry: A Proof of Concept**

Joseph M. DeCunha, Fernanda Villegas, Martin Vallières, Jose Torres, Sophie Camilleri-Broët, Shirin A. Enger

The histopathological samples presented in Chapter 2 of this thesis were extracted and processed by Dr. Torres, Dr. Camilleri-Broët, Dr. Rayes, and Dr. Spicer. The histopathological sample presented in Chapter 3 of this thesis was extracted and contoured by Dr. Camilleri-Broët. The software used for cell and nucleus size extraction from histopathological samples was developed in part by Dr. Vallières and Dr. Poole. Components of the Monte Carlo user code utilized in Chapter 3 were developed by Dr. Poole. Dr. Villegas contributed immensely to the written preparation and methodological approach of Chapter 3.

## Table of Contents

### I. Introduction and Theory

#### I.I Microdosimetry

I.I.I Quantities in Microdosimetry

I.I.II Regional vs. Structural Microdosimetry

I.I.III Probability Density Functions

I.I.IV Determination of  $f(z,D)$  by Convolution

I.I.V Target size in Microdosimetry

I.I.VI Suitability of Condensed History Physics Models for Microdosimetry

#### I.II Radiobiological Models in Clinical Use

I.II.I The Utility of Radiobiological Models

I.II.II The Parameters  $\alpha$  and  $\beta$

I.II.III Microdosimetric Kinetic Model

I.II.IV Local Effect Model

#### I.III Whole Slide Image Analysis

I.III.I Hematoxylin and Eosin Stained Histopathological Samples

I.III.II Stain Deconvolution

I.III.III Difference of Gaussians Method for Blob Detection

### II. Development of Patient-Specific 3D Models from Histopathological Samples for Investigations in Radiation Therapy

#### II.I Introduction

#### II.II Aims

#### II.III Methods

#### II.IV Results

#### II.V Discussion

#### II.VI Conclusion

### III. Patient-Specific Microdosimetry

#### III.I Introduction

#### III.II Aims

#### III.III Methods

III.IV Results

III.V Discussion

III.VI Conclusion

IV. Further Areas of Investigation

IV.I Target Spacing Dependence of Microdosimetric Distributions

IV.II Inter-patient Variation in Radiosensitivity

IV.III Cell Cycle Dependence of Radiosensitivity to DNA DSB Induction

IV.IV Calculation of S-values in Radiopharmaceutical Therapy

V. Conclusions

## Chapter I: Introduction

### I.I Microdosimetry

#### I.I.I Quantities in Microdosimetry

Microdosimetry is the study of statistical distributions of energy deposition by ionizing radiation in microscopic targets; typically to quantify the anticipated biological effects of an irradiation. Formal definitions of quantities used in microdosimetry have been established in the International Commission on Radiation Units and Measurements (ICRU) reports 36 and 85a [1-2]. Single energy deposition events by ionizing radiation can be described in terms of the quantity energy deposit,  $\epsilon_i$ :

$$\epsilon_i = \epsilon_{in} - \epsilon_{out} + Q \quad (1 - 1)$$

Where  $\epsilon_{in}$  is the kinetic energy of the incident ionising particle,  $\epsilon_{out}$  is the kinetic energy of all particles exiting the interaction, and  $Q$  is the change in rest mass energy of all elementary particles involved in the interaction. A quantity energy imparted,  $\epsilon$ , is then the summation of energy deposit within a volume:

$$\epsilon = \sum \epsilon_i \quad (1 - 2)$$

Macroscopic quantities used to describe energy deposition of ionizing radiation are in fact expectation values of quantities which are randomly distributed on the microscopic level [3]. One such quantity is the absorbed dose,  $D$ , which is defined:

$$D = \frac{d\bar{\epsilon}}{dm} \quad (1 - 3)$$

where  $d\bar{\epsilon}$  is the expectation value of energy imparted to a region and  $dm$  is the mass of that macroscopic region. The random variable corresponding to absorbed dose, is denoted the specific energy,  $z$ :

$$z = \frac{\epsilon}{m} \quad (1 - 4)$$

where  $\epsilon$  is the exact energy imparted to a volume and  $m$  the mass of that volume. Similarly, the macroscopic quantity of unrestricted linear energy transfer (LET) is defined as:

$$L_{\infty} = \frac{dE}{dx} \quad (1 - 5)$$

where the average energy transfer by a track of ionizing radiation is,  $dE$ , while traversing a distance,  $dx$ . Much like specific energy is the microscopic analog of absorbed dose, lineal energy,  $y$ , is a microscopic analog of LET. Lineal energy is defined as the quotient of total energy imparted to a volume,  $d\epsilon$ , and the mean chord length through that volume,  $L$ , giving:

$$y = \frac{d\epsilon}{L} \quad (1 - 6)$$

Lineal energy and LET are both physical parameters which through modelling can give an indication of the yield of biological damage for a given absorbed dose of ionizing radiation (i.e. the biological effectiveness of an irradiation) [3].

### **I.I.II Regional vs. Structural Microdosimetry**

The field of microdosimetry can be broadly grouped into two distinct branches: *regional microdosimetry* and *structural microdosimetry*, this categorization was popularized by the comprehensive 1996 work of Zaider and Rossi [4]. The quantities introduced thus far have primarily pertained to regional microdosimetry, which involves energy depositions in targets of defined sizes. Structural microdosimetry concerns itself with the inherent structure of energy deposition by ionizing radiation at the micro or nanoscopic level. One such example of structural microdosimetry is presented in the work of Bäckström *et al.* (2013) in which clusters are defined as a series of energy deposition points each linked to another through energy depositions spaced less than a distance  $d_c$  apart [5]. An extension of the previous work by Bäckström successfully

correlates cluster order, which is the number of energy depositions in a single cluster, with radiobiological parameters [6].

There is not a fundamental tension between structural and regional microdosimetry regarding which branch will yield the information most useful for biological modelling. Increasingly, the paradigm being adopted is that a complete mechanistic understanding of a biological system's response to irradiation will require information relevant to the macro, micro, and nanoscale interactions of ionizing radiation which may include information from both branches of microdosimetry. Additionally, values in regional microdosimetry may be correlated with, or provide a fast approximate method to determine values of interest in structural microdosimetry.

### **I.I.III Probability Density Functions**

Information in microdosimetry is typically represented by probability density functions (PDFs). A PDF denoted by  $f(x)$  yields the probability of an event occurring whose value is between  $x$  and  $x + dx$  [3]. Or, more intuitively, integration of a PDF corresponds to the probability of an event occurring between the bounds of integration. PDFs respect the property of normalizability such that:

$$\int_{-\infty}^{\infty} f(x) dx = 1 \quad (1 - 7)$$

The average value or expectation value of any given PDF is given by:

$$\bar{x} = \int_{-\infty}^{\infty} f(x) \cdot x dx \quad (1 - 8)$$

PDFs are used to describe lineal and specific energy deposition probabilities. The function  $f(y)$  represents the probability density of a volume receiving an amount of lineal energy when a single track of ionizing radiation deposits energy within it. A related function  $d(y)$ , characterizes the fractional amount of dose delivered to a volume by tracks of a given lineal energy. The mean or

expectation values of each function are known as the frequency mean lineal energy ( $\bar{y}_f$ ) and dose mean lineal energy ( $\bar{y}_d$ ) respectively. The lineal energy dose distribution is related to the lineal energy frequency distribution through:

$$d(y) = \frac{y}{\bar{y}_f} f(y) \quad (1 - 9)$$

An analogous set of frequency and dose distribution functions to those introduced for lineal energy exist for specific energy. The expectation values of the frequency and dose distributions are also called the first and second moments of the distributions, respectively.

A particularly versatile PDF in microdosimetry is the single-event specific energy distribution,  $f_1(z)$ .  $f_1(z)$  is a function representing the probability density of a volume receiving an amount of specific energy when a single track of ionizing radiation deposits energy within it. A power of  $f_1(z)$  lies in its ability to encode a diversity of microdosimetric information when various statistical properties are exploited. As the amount of energy imparted from one track of ionizing radiation to a target is typically independent of any energy deposited by a later incident particle, the probability distribution of specific energy for a target hit by two tracks of ionizing radiation is given by a convolution of  $f_1(z)$  with itself:

$$f_2(z) = f_1(z) \otimes f_1(z) \quad (1 - 10)$$

This is generalizable to a target hit by N tracks of ionizing radiation:

$$f_N(z) = f_{N-1}(z) \otimes f_1(z) \quad (1 - 11)$$

The microdosimetric function  $f_1(z)$  readily encodes information about irradiation by an arbitrarily large number of particles. This property makes determination of microdosimetric functions which would otherwise be unfathomable using typical experimental or computational methods possible.

### I.I.IV Determination of $f(z,D)$ by Convolution

A function that denotes the variation in specific energy between targets when a given absorbed dose level is achieved is denoted  $f(z, D)$  [4].  $f(z, D)$  can be represented by a summation of  $f_N(z)$ 's. This is very useful, as when  $D$  and  $f_1(z)$  are known, information from the two can be used to describe the total variation in energy deposition in targets of interest at a given absorbed dose level. The calculation of  $f(z, D)$  will be described later in this chapter. The expectation value of the single event specific energy frequency distribution is given by:

$$\bar{z}_1 = \int_{-\infty}^{\infty} f_1(z) \cdot z \, dz \quad (1 - 12)$$

$\bar{z}_1$  is known as the single event frequency mean specific energy, which corresponds to the average specific energy imparted in a volume when a single track of ionizing radiation interacts with it. If the absorbed dose to a region is known along with  $\bar{z}_1$  the mean number of events necessary to accumulate the absorbed dose in that volume is calculable:

$$\bar{n} = \frac{D}{\bar{z}_1} \quad (1 - 13)$$

where  $\bar{n}$  is known as the mean event frequency. Because individual tracks of ionizing radiation are independent of one another, the probability of the number of energy deposition events occurring in a volume is given by a Poisson distribution with mean  $\bar{n}$ .

$$p(n) = \frac{\bar{n}^n e^{-\bar{n}}}{n!} \quad (1 - 14)$$

Given that the probability of  $n$  events occurring in a volume is characterized, and the associated specific energy distribution for each number of events can be determined through convolution,  $f(z, D)$  can be readily determined:

$$f(z, D) = \sum_{n=0}^{\infty} p(n) \cdot f_n(z) \quad (1 - 15)$$

Distributions of  $f(z, D)$  have been used in order to place an upper limit on the biological target size of interest from observed biological outcomes [7].  $f(z, D)$  has also been used for dosimetry of alpha emitting radioisotopes [8].

#### **I.I.V Target size in Microdosimetry**

Given that all values in regional microdosimetry are calculated in targets of a given size, establishing the biological target size of interest is of great importance to ensure that microdosimetric energy distributions obtained are relevant to the biological system under consideration. Some studies attempt to invert the problem, by establishing the target size whose microdosimetric distributions correlate most closely with a biological endpoint to determine the relevant biological target size [7,9]. Traditionally, research in regional microdosimetry has considered energy deposition in targets of a single size. This study of microscopic energy deposition conflicts with a more intuitive understanding which suggests that microdosimetric energy depositions should be determined in a distribution of target sizes, as biological targets in living tissues vary in size throughout the cell cycle and between cancer types [10-11]. Recent work by Oliver *et al.* (2018) indicates that  $f(z, D)$  distributions determined in a variety of target sizes demonstrate greater microdosimetric spread than those determined in a single target size alone [12]. Evidently, regional microdosimetry in targets whose size distributions are determined from patient tissues may yield more relevant information than current microdosimetric distributions determined in fixed targets of approximate sizes.

#### **I.I.VI Suitability of Condensed History Physics Models for Microdosimetry**

The Monte Carlo (MC) method has a long history of use for the computation of numerical solutions to equations of radiation transport, dating back at least as far as 1947 [13]. Broadly speaking, the MC method is a statistical approach for the determination of solutions to integro-differential

equations [14]. Due to the difficulty of direct measurement of microscale and nanoscale interactions of ionizing radiation, computational approaches to determination of quantities in microdosimetry have and continue to be actively employed [4]. An expansive number of software toolkits have been developed which allow an end user to determine solutions to equations of radiation transport using MC methods, these toolkits include: EGS, Geant4, MCNP, Penelope, FLUKA, KURBUC, PARTRAC, and many others [15-21].

When MC methods are used for the computation of ionizing radiation transport of electron and photon emitting sources in medical radiation physics, a series of physics models known as condensed history (CH) models are typically used. CH models involve splitting a simulated track of ionizing radiation into a series of discrete steps [22]. In the CH method, track steps are a computational abstraction and have no physical interpretation. In between track steps there are discrete locations where the total energy deposition and net change in angular momentum of the particle under investigation are calculated by the use of a multiple-scattering theory. The advantage of the CH approach is that it improves the computational efficiency of MC methods in radiation therapy by orders of magnitude compared to track-structure (TS) approaches which attempt to calculate singular interactions of an ionizing particle without the use of a multiple-scattering theory. Given that knowledge of the nanoscale interactions of ionizing radiation is not typically of interest for many macroscopic investigations, the loss of spatial resolution which occurs when using CH models is often insignificant.

In microdosimetry, where an accurate understanding of the energy deposition patterns of ionizing radiation on the micro and nanoscales is desired, multiple-scattering theories do not always provide a suitable approximation of microscopic energy deposition [23]. Because of the computational efficiency advantages of CH methods, investigations have been conducted to determine for which

energy and size domains the results of CH and TS MC calculations yield similar results. Attempts have been made to determine whether a particular set of input parameters to CH methods (i.e. secondary electron tracking cutoff, step length) can yield microdosimetric distributions in nanoscale volumes which are comparable to TS approaches [24]. Attempts to use CH methods to approximate the microdosimetric distributions determined using TS codes has had varying levels of success in spheres of diameter 100 nm or smaller. There is strong evidence that in spheres of diameter 300 nm and larger the microdosimetric results yielded by CH methods are equivalent to those yielded by TS simulations in Geant4 [25].

## **I.II Radiobiological Models in Clinical Use**

### **I.II.I The Utility of Radiobiological Models**

Broadly speaking, radiobiological models refer to any mathematical formulation which correlates a property of an irradiation including the radiation quality, duration of radiation exposure, and number of irradiations with the biological effect of such an irradiation. Evidently radiobiological models must be dependent on biological parameters in addition to physical ones. The overview presented here specifically limits itself to radiobiological models which are in current clinical use and which require microdosimetric inputs. Radiobiological models which receive microdosimetric inputs and have been used in clinical practice include: the microdosimetric kinetic model (MKM), modified microdosimetric kinetic model (MMKM), and the Local Effect Model (LEM) [26-28].

The relative biological effectiveness (RBE) refers to the ratio of absorbed dose from an experimental and reference source of radiation in order to achieve the same biological effect for a given endpoint:

$$RBE = \frac{D_{EXP}}{D_{REF}} \text{ (same endpoint)} \quad (1 - 16)$$

Typically, radiobiological models yield an expected value of RBE or parameters which can then be used to calculate RBE. The earliest work to discuss the potential connections of lineal energy to the RBE of an irradiation was the foundational 1960 work of Harold Rossi [29]. Early attempts to qualitatively explain the biological effectiveness of an irradiation in terms of microscopic patterns of energy deposition have origins in the early 20th century [30]. While methods to incorporate observable microdosimetric quantities into models describing biological damage were developed much later [31].

Knowledge of the RBE for a given radiation quality has been essential to the use of ions in radiotherapy [28]. Carbon and proton therapies are planned with knowledge of the RBE for cell death relative to MeV photon therapies. This allows ion therapies to be planned using the extensive quantity of outcome data which has been accumulated from decades of treatment with MV photons. As the reference therapy, the RBE of MV photon therapies are typically taken to be 1. For carbon therapy the spatially varying RBE (approaching 5 in the Bragg peak region) is considered while a fixed RBE of 1.1 is adopted for proton therapy [28,32]. In addition to ion therapies, knowledge of RBE is also important in the planning of treatments with low energy photon emitting brachytherapy sources such as  $^{125}\text{I}$  and  $^{103}\text{Pd}$  and low energy x-ray sources for which an enhancement in RBE is observed with decreasing photon energy [33-40]. Furthermore, increased RBE of low energy photons has important implications for understanding the risks associated with mammography screening programs [41]. Innovations in brachytherapy, such as investigating novel isotopes for use in conventional or intensity-modulated brachytherapy also necessitate further microdosimetric and radiobiological studies [42-48]. Much of the interest in microdosimetry has been sustained by a desire to precisely quantify the anticipated biological effectiveness of each of these therapies.

A specific subcategory of radiobiological model which only models the varying biological effectiveness of an irradiation depending on absorbed dose level and number of irradiations is known as a fractionation model. While in principle many radiobiological models can model variation in RBE due to fractionation and other factors, in practice fractionation models are typically applied separately.

### I.II.II The Parameters $\alpha$ and $\beta$

An empirical model which underlies most models of radiation dose response is the linear quadratic model (LQ) [49]. The LQ model states that the logarithm of the surviving fraction of cells after exposure to an absorbed dose of radiation is proportional to the sum of the absorbed dose and the square of the absorbed dose:

$$-\ln(S) = \alpha d + \beta d^2 \quad (1 - 17)$$

Where  $\alpha$  and  $\beta$  are proportionality constants for the linear and quadratic contributions of the absorbed dose to the surviving fraction respectively. The LQ model has been successfully applied to other endpoints than cell survival as well [50-51]. If the ratio of the LQ model is taken and rearranged, a statement for the RBE of a treatment in terms of  $\alpha$  and  $\beta$  parameters and absorbed dose can be derived:

$$RBE(D) = \frac{(\alpha_R/\beta_R)}{2D} \left\{ -1 + \sqrt{1 + \frac{4D}{(\alpha_R/\beta_R)} \left( 1 + \frac{D}{(\alpha_R/\beta_R)} \cdot \frac{\beta_{exp}}{\beta_r} \right) \alpha_{exp}/\alpha_R} \right\} \quad (1 - 18)$$

Where  $\alpha_R$  and  $\beta_R$  are LQ model parameters for the reference radiation source and  $\alpha_{exp}$  and  $\beta_{exp}$  are LQ model parameters for the source of interest [52].

An intuitive interpretation of the LQ model has been a matter of some debate [53]. A possible mechanistic interpretation of the linear and quadratic parameters include the explanation that they

arise as the result of lethal damage from single and multiple tracks respectively. A competing, but related explanation is that the linear component of the LQ model arises as the result of lethal damage to the cell and the quadratic component from sublethal or unrepaired lesions [54-55]. Others posit that the LQ model is nothing more than an empirical model rather than a mechanistic one.

If fractions of ionizing irradiation are assumed to be delivered far enough apart that all sublethal damage is repaired and radiosensitivity is assumed to remain constant throughout a treatment, the LQ model can be used to predict cell survival after several fractions of ionizing radiation are delivered. This makes the LQ model with assumptions a form of fractionation model and is the basis for the concept of isoeffective dose (EQD) and biologically effective dose (BED) [56-57].

### **I.II.III Microdosimetric Kinetic Model**

A particularly influential mechanistic model which describes the time-varying processes of cellular damage repair and can take inputs from observable microdosimetric quantities is the MKM developed by Hawkins [26]. The MKM is described by a set of linked ordinary differential equations (ODEs) which describe the time variation of reparable and irreparable lesions:

$$\dot{x}_d = k_d \dot{G}_d - (a + c)x_d - 2b_d x_d^2 \quad (1 - 19)$$

$$\dot{x}_{ad} = \lambda_d \dot{G}_d + ax_d + b_d x_d^2 \quad (1 - 20)$$

Where  $x_d$  and  $x_{ad}$  are the number of reparable and irreparable lesions respectively,  $a$  and  $b_d$  are first and second order rate constants for the generation of irreparable lesions from reparable lesions,  $c$  is the first order repair constant, and  $k_d$  and  $\lambda_d$  are the yield parameters of reparable and irreparable lesions per unit dose. If  $\lambda_d$  is taken to be zero the MKM reduces to the repair misrepair model and similarly the MKM reduces to the lethal potentially-lethal model if  $a$  is zero [54-55].

Evidence supporting the mechanistic description of damage from ionizing radiation provided by the MKM is presented in the 1996 work by Hawkins in which solutions to the ODEs presented yield functional forms compatible with cell survival relations observed experimentally [26].

The MKM kinetic equations are almost never applied directly. In practice, solutions to MKM kinetic equations are used to yield more useful relations in terms of measurable parameters such as  $\alpha$ ,  $\beta$ , and LET. Most applications of the MKM assume  $\beta$  is independent of radiation quality [58]. The MKM can be configured to yield predictions of  $\alpha$  for an arbitrary radiation quality, given  $\alpha$  and  $\beta$  of a reference radiation quality and  $f(y)$  in nuclei and in nanometer scale sub-compartments of the nucleus known as domains. A domain is conceptualized as the largest possible volume in the nucleus in which two independent repairable lesions of biological damage can combine to form an irreparable lesion; any biological damage existing in a domain is “invisible” to damage in other domains. The MKM has been further developed by Hawkins and others in response to disagreements between the model and measured biological data [59]. A particular modification of the MKM, the MMKM has been used clinically in Japan to predict the varying RBE of carbon ion treatments [27]. Various implementations of the MKM require  $\bar{y}_d$ ,  $f(y)$ , or  $d(y)$  as a necessary input parameter to predict the biological effectiveness of an irradiation.

#### **I.II.IV Local Effect Model**

The LEM is a radiobiological model which is used clinically to predict RBE of carbon ion therapies [60]. Four iterations of the LEM have been proposed and the most recent and advanced, LEM IV will be described here [28,61-63]. Unlike the MKM, the LEM makes no attempt to model the repair kinetics of biological damage from ionizing radiation. The LEM assumes that only the initial distribution of energy imparted, or the initial yield of DNA double strand breaks (DSBs) by the

energy imparted are relevant to the determination of RBE between two sources of ionizing radiation.

An idea fundamental to the LEM and from which it retrieves its name is the concept of local dose. Analogous to the concept of the domain in the MKM, cubic nucleus domains of 540 nm side length which are meant to correspond to a chromatin subunit are modelled in the LEM. The LEM states that dose locally deposited in domains of the nucleus yield an equivalent amount of local biological damage regardless of the radiation quality. Also like the MKM, biological damage in separate domains are not thought to interact with each other. In practice, tracks of ionizing radiation are computationally superimposed over models of the nucleus. The energy imparted by tracks of ionizing radiation is then considered a probability distribution for induction of DNA DSBs and sampled from randomly. Patterns of DNA DSBs are then determined in as many as  $10^6$  independent nucleus models to achieve appropriate statistical uncertainties. A concept known as the cluster index,  $C$ , is then determined for both the reference and experimental radiation quality:

$$C = \frac{N_{cDSB}}{N_{iDSB} + N_{cDSB}} \quad (1 - 21)$$

Where  $N_{cDSB}$  are the number of domains in a nucleus containing clustered (more than 1) DSB, and  $N_{iDSB}$  are the number of domains in a nucleus containing individual DSBs. The dose at which the reference photon radiation quality has the same cluster index as the experimental radiation quality at dose  $D$ , is determined and denoted  $D_{eq}$ . Typically, the radiation quality for which determination of RBE is desired will be much more densely ionizing than the reference radiation quality. Thus, the dose required for the reference photon radiation quality to deliver an equivalent cluster order as the experimental radiation quality, will be much larger than the dose of the experimental radiation quality. The ratio of the total number of DSBs per nucleus generated by the experimental

radiation quality at dose  $D$  and the reference radiation quality at dose  $D_{eq}$  is denoted by  $\kappa$  [64]. With knowledge of  $D_{eq}$  and  $\kappa$ , the LEM posits that the survival fraction for the experimental radiation quality can be directly determined from the survival curve of the reference radiation quality, with appropriate scaling:

$$S_{Exp}(D) = S_{\gamma}(D_{eq}) \cdot e^{\kappa} \quad (1 - 22)$$

Where  $S_{Exp}$  is the survival fraction of the experimental radiation quality and  $S_{\gamma}$  is the survival fraction of the reference photon radiation quality. An advantage of the LEM over the MKM is that it does not require any biological input data from irradiations conducted using the experimental radiation quality as all biological information is inferred from the reference photon survival curve (Figure 1-1).

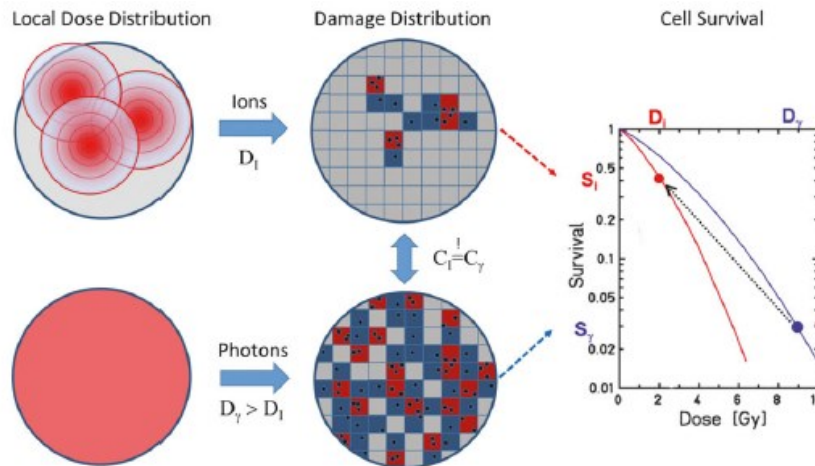


**Figure 1-1:** (Left) An illustration depicting an ion and photon irradiation with an equivalent cluster index. (Right) A diagram depicting the retrieval of the survival curve after ion irradiation (red) from a survival curve after photon irradiation (blue). The dashed black line represents scaling of the surviving fraction at  $D_{eq}$  by a factor of  $\kappa$ . Image extracted from [52].

A notable difference exists between the MKM and LEM regarding the values of  $\beta_{exp}$  yielded by each model. In the MKM  $\beta$  is thought to be a biological property alone and independent of the radiation quality investigated, and thus is constant for all radiation qualities. Conversely, in the

LEM  $\beta_{exp}$  is predicted to decrease with increasing LET of the experimental radiation quality. A comprehensive description of differing predictions made by the MKM and LEM and potential investigations which could determine the more accurate radiobiological model are described in the 2018 work of Stewart *et al* [52].

### **I.III Whole Slide Image Analysis**

#### **I.III.I Hematoxylin and Eosin Stained Histopathological Samples**

A tissue microarray (TMA) is a method in pathology which allows for high throughput analysis of histologic data [65]. Physically, a TMA is thin paraffin block in which individual tissue samples, typically extracted from patients are embedded (Figure 1-2). The individual tissue samples are commonly extracted using a hollow-core needle in a procedure referred to as a biopsy. Tissue samples at different lateral distances along the extraction needle will be embedded in a TMA to give information about the spatial variation of disease. A TMA will usually contain information from needle extractions taken at several locations where the presence of a tumour is suspected in a single patient and also information for several patients. The completed TMA can then be sliced axially to produce 10-50 copies of the information to be used for different analyses. Analyses performed on TMAs include but are not limited to fluorescence in-situ hybridization for detection of targeted genetic markers, immunohistochemistry for detection of immunomarkers, or more conventional techniques such as staining with Hematoxylin and Eosin (H&E) for later observation and analysis by a pathologist.

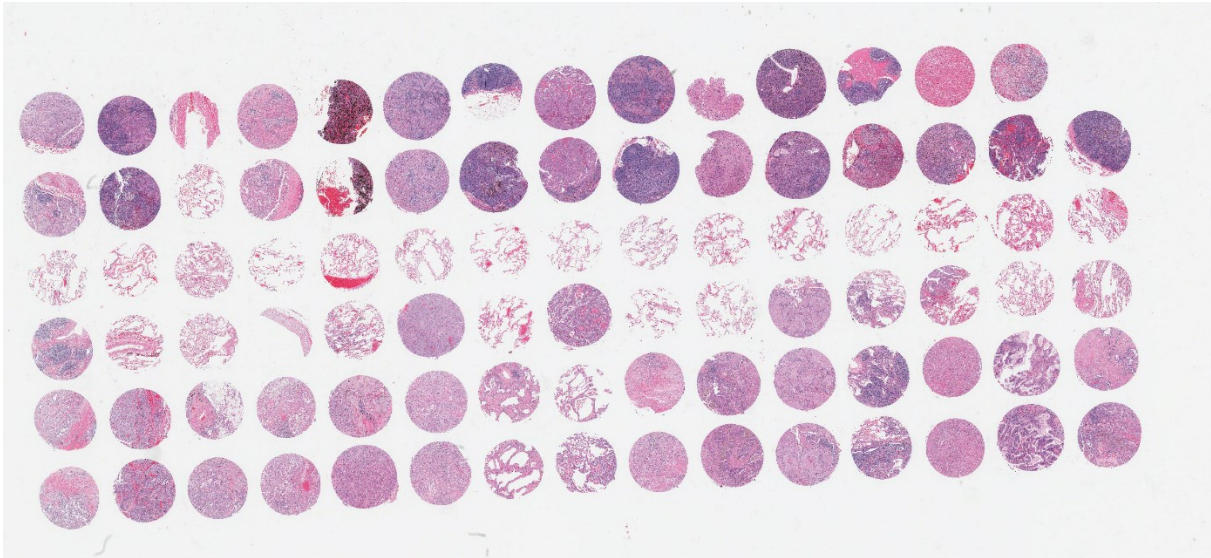


**Figure 1-2:** Digital light-field microscopy image of a TMA containing 90 samples from suspected non-small cell lung carcinoma patients gathered at the McGill University Health Center.

H&E are the most common stains used to generate contrast on histopathological samples [66]. Both hematoxylin and eosin are typically used together in the staining process, as each stain reveals differing and complementary structures. Hematoxylin must undergo oxidation from its raw extracted form in order to be developed into the active dye Hematein. Hematein has a poor inherent affinity to bind with tissue and thus a complementary chemical known as a mordant is often introduced to increase the binding efficiency of the stain. Common mordants for hematein include aluminum potassium sulfate, iron, tungsten, and molybdenum [67]. The mordant utilized can change the uptake and colour properties of the stain.

Regardless of the mordant employed hematoxylin derived stains are each attracted to and stain the same structures. Structures stained by hematein include ribonucleic acid (RNA), deoxyribonucleic acid (DNA), ribosomes, and the rough endoplasmic reticulum which are dyed shades of purple or blue [68]. Structures stained by eosin are referred to as eosinophilic and include the cell membrane, various proteins, mitochondria, and other connective structures which are dyed pink. Hematoxylin

derived stains tend to provide information about structures within the cell nucleus, while eosin stains provide information regarding structures outside of the nucleus.

### **I.III.II Stain Deconvolution**

With the advent of digital pathology, high resolution scanned images of histopathological samples can be retrieved and analyzed [67]. Digitally scanned complete histopathological samples are referred to as whole slide images (WSI). WSIs of H&E stained pathology slides aim to recreate the image generated under observation in light-field microscopy where visible white light is emitted through the sample towards the observer. Both the advent of digital pathology and of standards developed by regulation authorities to reduce variability in H&E stains have allowed for reliable quantitative data to be extracted from H&E stained pathology slides. In many cases where quantitative data is to be extracted from H&E stained samples it is necessary to isolate the contribution of hematoxylin and eosin to the colour content in an image separately. For quantification of the size or shape of nuclei present in a H&E stained sample only knowledge of hematoxylin stained regions is of value, as eosin does not confer information about nuclear regions [69]. The representation of an H&E stained sample as a summation of two basis images composed of its constituent stains is known as stain deconvolution.

Numerous methods for deconvolution of H&E stain containing samples have been proposed [70]. Two predominant methods for stain deconvolution of H&E samples exist, a method proposed by Ruifrok *et al.* in 2003 and a method proposed by Macenko in 2009 [71-72]. The method proposed by Ruifrok *et al.* assumes that the concentration of a stain contributes linearly to the optical density of a pixel and is applicable to a slide containing an arbitrary number of stains. While the method proposed by Macenko uses histograms of the color information present in a slide in order to develop distinct hematoxylin and eosin colour vectors. An optimization algorithm is then

conducted on a pixelwise basis to determine which summation of colour vectors most closely matches the pixel's colour value. Sources of inter-image variation including staining protocols, stain composition, stain deterioration with age, and imaging equipment can affect the colour composition of a WSI and confound stain deconvolution methods. For this reason both the techniques devised by Ruifrok and Macenko see continued development to improve the generalizability of each method [73-74]. In more restricted sets of stained samples with little inter-image variation less robust methods of stain separation including simple thresholding may prove adequate.

### **I.III.III Difference of Gaussians Method for Blob Detection**

In addition to quantitative information regarding the quantity and concentration of stain present in a WSI it may be of interest to identify the locations of cells or nuclei present in an image. If an accurate mapping of cell locations are determined, the amount of stain associated with each cell can be determined in order to characterize various cell properties. A subset of feature detection techniques known as blob detection algorithms are methods which seek to extract continuous regions of an image which share a similar arbitrary trait. Numerous blob detection algorithms exist and may be suitable for the determination of nuclei present in a hematoxylin stained WSI [75]. One such blob detection technique is known as the Difference of Gaussians (DoG) method. The DoG method received widespread use as the first step in the scale invariant feature transform (SIFT) which is an extremely common algorithm in computer vision [76-77].

The DoG method for blob detection involves repeated convolutions of an image with a two-dimensional gaussian function (known as the kernel). The standard deviation of the gaussian kernel is varied for each convolution of the image, with greater standard deviations yielding an image that is more blurred after convolution and smaller standard deviations the opposite. The many

convolved images of different levels of blurriness are then stacked into a three-dimensional matrix by order of gaussian kernel standard deviation [78]. Local maxima in the three-dimensional matrix are said to be scale invariant and correspond to features present in the image. The extrema of the gaussian kernel standard deviation and the threshold of local maxima present in the matrix can be tuned for more accurate operation of the algorithm.

## References

- [1] Booz J, Braby L, Coyne J, et al. Microdosimetry (ICRU Report 36). *J. ICRU*. 1983;19(1).
- [2] ICRU (International Commission on Radiation Units & Measurements). Report 85a revised: Fundamental quantities and units for ionizing radiation. *J. ICRU* 2011; 11(1).
- [3] Lindborg L, Waker A. Microdosimetry: Experimental Methods and Applications. Boca Raton, USA, CRC Press, 2017.
- [4] Rossi H.H, Zaider M. Microdosimetry and Its Applications. Berlin, Germany, Springer-Verlag, 1996.
- [5] G. Bäckström, Protons, Other Light Ions, and  $^{60}\text{Co}$  Photons: Study of Energy Deposit Clustering Via Track Structure Simulations (Acta Universitatis Upsaliensis, Uppsala, 2013).
- [6] Villegas F, Bäckström G, Tilly N, *et al.* Energy deposition clustering as a functional radiation quality descriptor for modelling relative biological effectiveness. *Med. Phys.* 2016;43(12):6322-6335.
- [7] Villegas F, Tilly N, Ahnesjö A. Target Size Variation in Microdosimetric Distributions and its Impact on the Linear-Quadratic Parameterization of Cell Survival. *Radiat. Res.* 2018;190(5):504-512.
- [8] Palm S, Humm J.L, Rundqvist R, *et al.* Microdosimetry of astatine- 211 single-cell irradiation: Role of daughter polonium-211 diffusion. *Med. Phys.* 2004; 31(2):218-225.
- [9] Scalliet P and Wambersie A. Which RBE for iodine 125 in clinical applications? *Radiother Oncol* 1987;9:221-230.
- [10] Maeshima K, Iino H, Hihara S, *et al.* Nuclear size, nuclear pore number and cell cycle. *Nucleus* 2011;2(2):113-118.
- [11] Zink D, Fischer A.H, Nickerson J.A. Nuclear Structure in Cancer Cells. *Nat. Rev. Cancer* 2004;4:677-687.

- [12] Oliver P.A.K, Thomson R.M. Investigating energy deposition within cell populations using Monte Carlo simulations. *Phys. Med. Biol.* 2018;63(15):155018.
- [13] Richtmyer, R.D., von Neumann, J. Statistical methods in neutron diffusion. Los Alamos Scientific Laboratory Report LAMS-551. Los Alamos 1947.
- [14] Vassiliev, O.N. Monte Carlo methods for radiation transport : fundamentals and advanced topics. Cham: Springer, 2016.
- [15] Ford, R.L, Nelson, W.R. The EGS code system: computer programs for the Monte Carlosimulation of electromagnetic cascade showers (Version 3). Stanford Linear Accelerator Center, Report 210, Stanford 1978.
- [16] Agostinelli, S, Allison, J, Amako, K, *et al.* Geant4 – a simulation toolkit. *Nucl. Inst. Methods A* 2003;506(3):250–303.
- [17] Brown F.B. MCNP – a general Monte Carlo N-particle transport code, version 5. Los Alamos National Laboratory Report LA-UR-03-1987, Los Alamos 2003.
- [18] Salvat, F, Fernandez-Varea J.M, Sempau, J. Penelope-2011: A Code System for Monte Carlo Simulation of Electron and Photon Transport (Workshop Proceedings). Issy-les-Moulineaux, OECD/NEA Data Bank, France 2011.
- [19] Böhlen T.T, Cerutti F, Chin M.P.W, *et al.* The FLUKA Code: Developments and Challenges for High Energy and Medical Applications. *Nucl. Data Sheets* 2014;120:211-214.
- [20] Nikjoo H, Emfietzoglou D, Liamsuwan T, *et al.* Radiation track, DNA damage and response-a review. *Rep. Prog. Phys.* 2016;79:116601.
- [21] Friedland W, Dingfelder M, Kundrat P, *et al.* Track structures, DNA targets and radiation effects in the biophysical Monte Carlo code PARTRAC. *Mutat Res.* 2011;711:28–40.
- [22] Berger, M.J. Monte Carlo calculations of the penetration and diffusion of fast charged particles. *Methods in Computations Physics*, Vol 1 1963. New York: Academic Press, 135-215.
- [23] Bernal M.A, Liendo J.A. An investigation on the capabilities of the PENELOPE MC code in nanodosimetry. *Med. Phys.* 2009;36(2):620-625.
- [24] Lazarakis P. Influence of track structure and condensed history physics models of Geant4 to nanoscale electron transport in liquid water. *Biomed. Phys. Eng. Express* 2018;4:024001.
- [25] Kyriakou I, Emfietzoglou D, Ivanchenko M, *et al.* Microdosimetry of electrons in liquid water using the low-energy models of Geant4. *Jour. Appl. Phys.* 2017;122:024303.
- [26] Hawkins R.B. A microdosimetric-kinetic model of cell death from exposure to ionizing radiation of any LET, with experimental and clinical applications. *Int. J. Radiat. Biol.* 1996;69(6):739-755.

- [27] Inaniwa T, Furukawa T, Kase Y, Matsufuji N, Toshito T, Matsumoto Y, Furusawa Y, Noda K. Treatment planning for a scanned carbon beam with a modified microdosimetric kinetic model. *Phys Med Biol*. 2010;55:6721–6737.
- [28] Elsässer Y, Weyrather W.K, Friedrich T, *et al*. Quantification of the relative biological effectiveness for ion beam radiotherapy: direct experimental comparison of proton and carbon ion beams and a novel approach for treatment planning. *Int. J. Radiat. Oncol. Biol. Phys.* 2010;78(4):1177-1183.
- [29] Rossi H.H. Spatial Distribution of Energy Deposition by Ionizing Radiation. *Radiat Res Supp*. 1960. 2:290-299.
- [30] Crowther J.A. Some Considerations Relative to the Action of X-Rays on Tissue Cells. *Proc. R. Soc. B* 1924. 96:207-211.
- [31] Kellerer A. M., Rossi H.H. Theory of Dual Radiation Action. *Curr. Top. Radiat. Res.* 1972; 8:85-158.
- [32] Paganetti H, Blakely E, Carabe-Fernandez A. Report of the AAPM TG-256 on the relative biological effectiveness of proton beams in radiation therapy. *Med. Phys.* 2019;46(3):e53-e78.
- [33] Nikjoo H, Lindborg L. RBE of low energy electrons and photons. *Phys. Med. Biol.* 2010;55:R65-R-109.
- [34] McDonald JC, Ma I, Zeitz L. Microdosimetric properties of encapsulated 125I and other photon sources. *Radiat Res* 1979.
- [35] Wu CS, Zaider M. A calculation of the relative biological effectiveness of 125I and 103Pd brachytherapy sources using the concept of proximity function. *Med Phys* 1998;25:2186-2189.
- [36] Wu CS, Kliauga P, Zaider M, *et al*. Microdosimetric evaluation of relative biological effectiveness for 103Pd, 125I, 241Am, and 192Ir brachytherapy sources. *Int J Radiat Oncol Biol Phys* 1996;36:689-697. 77:221-232.
- [37] Reniers B, Vynckier S, Verhaegen F. Theoretical analysis of microdosimetric spectra and cluster formation for 103Pd and 125I emitters. *Phys Med Biol* 2004;49:3781-3795.
- [38] Wu CS, Chen J. Calculated microdosimetric characteristics of 125I and 103Pd brachytherapy seeds at different depths in water. *Radiat Prot Dosimetry* 2006;122:506-508.
- [39] Hill MA. The variation in biological effectiveness of low energy x-rays and gamma rays with energy. *Radiat Prot Dosimetry* 2008;112:471-481.
- [40] Brenner DJ, Leu CS, Beatty JF, *et al*. Clinical relative biological effectiveness of low-energy x-rays emitted by miniature x-ray devices. *Phys Med Biol* 1999;44:323-333.

- [41] Mills C.E, Thome C, Koff D, *et al.* The Relative Biological Effectiveness of Low-Dose Mammography Quality X Rays in the Human Breast MCF-10A Cell Line. *Radiat. Res.* 2015;183:42-51.
- [42] Famulari G, Pater P, Enger S.A. Microdosimetric Evaluation of Current and Alternative Brachytherapy Sources – A Geant4-DNA Simulation Study. *Int. J. Radiat. Oncol. Biol. Phys.* 2017;100(1):270-277.
- [43] Ballester F, Granero D, Perez-Calatayud J, Venselaar JLM, Rivard MJ. Study of encapsulated <sup>170</sup>Tm sources for their potential use in brachytherapy. *Med Phys.* 2010;37(4):1629-1637.
- [44] Enger SA, D'Amours M, Beaulieu L. Modeling a Hypothetical Tm-170 Source for Brachytherapy Applications. *Med Phys.* 2011;38(10):5307-5310.
- [45] Enger SA, Fisher DR, Flynn RT. Gadolinium-153 as a brachytherapy isotope. *Phys Med Biol.* 2013;58(4):957-964.
- [46] Famulari G, Ulrich T, Armstrong A, *et al.* Practical aspects of <sup>153</sup>Gd as a radioactive source for use in brachytherapy. *Appl Radiat Isot* 2017;130:131-139.
- [47] Shoemaker T, Vuong T, Glickman H, Kaifi S, Famulari G, Enger SA. Dosimetric Considerations for Ytterbium-169, Selenium-75, and Iridium-192 Radioisotopes in High-Dose-Rate Endorectal Brachytherapy. *Int J Radiat Oncol.* 2019;105(4):875-883.
- [48] Song WY, Tanderup K, Pieters BR. *Emerging Technologies in Brachytherapy.* Boca Raton: CRC Press; 2017.
- [49] McMahan S.J. The linear quadratic model: usage, interpretation and challenges. *Phys. Med. Biol.* 2019;64.
- [50] Lea D.E, Catcheside D.G. The mechanism of the induction by radiation of chromosome aberrations in *Tradescantia*. *J. Genet.* 1942;44:216–245.
- [51] Zhou C, Jones B, Moustafa M, *et al.* Quantitative assessment of radiation dose and fractionation effects on normal tissue by utilizing a novel lung fibrosis index model. *Radiat. Oncol.* 2017;12:172-180.
- [52] Stewart R.D, Carlson D.J, Butkus M.P, *et al.* A comparison of mechanism-inspired models for particle relative biological effectiveness (RBE). *Med. Phys.* 2018;45(11):e925-e952.
- [53] Kirkpatrick J.P, Brenner D.J, Orton C.G. The linear-quadratic model is inappropriate to model high dose per fraction effects in radiosurgery. *Med. Phys.* 2009;36:3381–3384.
- [54] Tobias C.A. The repair-misrepair model in radiobiology: comparison to other models *Radiat. Res. Suppl.* 1985;8:S77–S95.

- [55] Curtis S.B. Lethal and potentially lethal lesions induced by radiation—a unified repair model. *Radiat. Res.* 1986 ;106:252–270.
- [56] Withers H R, Thames H D, Peters L.J. A new isoeffect curve for change in dose per fraction. *Radiother. Oncol.* 1983;1:187–191.
- [57] Barendsen G.W. Dose fractionation, dose rate and iso-effect relationships for normal tissue responses. *Int. J. Radiat. Oncol. Biol. Phys.* 1982 ;8:1981–1997.
- [58] Kase Y, Kanai T, Matsumoto Y, et al. Microdosimetric measurements and estimation of human cell survival for heavy-ion beams. *Radiat. Res.* 2006;166(4):629-638.
- [59] Hawkins R.B. A microdosimetric-kinetic model for the effect of non-Poisson distribution of lethal lesions on the variation of RBE with LET. *Radiat. Res.* 2003;160(1):61-69.
- [60] Kramer M, Scholz M. Rapid calculation of biological effects in ion radiotherapy. *Phys Med Biol.* 2006; 51:1959–1970.
- [61] Scholz M, Kellerer AM, Kraft-Weyrather W, et al. Computation of cell survival in heavy ion beams for therapy. The model and its approximation. *Radiat. Environ. Biophys.* 1997;36:59–66.
- [62] Elsasser T, Scholz M. Cluster effects within the local effect model. *Radiat. Res.* 2007;167:319–329.
- [63] Elsasser T, Kramer M, Scholz M. Accuracy of the local effect model for the prediction of biologic effects of carbon ion beams in vitro and in vivo. *Int. J. Radiat. Oncol. Biol. Phys.* 2008;71:866-872.
- [64] Friedrich T, Scholz U, Elsasser T, et al. Calculation of the biological effects of ion beams based on the microscopic spatial damage distribution pattern. *Int. J. Radiat. Biol.* 2012;88(1-2):103-107.
- [65] Jawhar N.M.T. Tissue Microarray: A rapidly evolving diagnostic and research too. *Ann. Saudi Med.* 2009;29(2):123-127.
- [66] Kleczek P, Jaworek-Korjakowska J, Gorgon M. A novel method for tissue segmentation in high-resolution H&E-stained histopathological whole-slide images. *Comput. Med. Imag. Grap.* 2020;79:101686.
- [67] Suvarna, S.K., Layton, C., Bancroft, J.D. Bancroft's theory and practice of histological techniques, 7th Edition. Churchill Livingstone (2013).
- [68] Chan J.K.C. The Wonderful Colors of the Hematoxylin–Eosin Stain in Diagnostic Surgical Pathology. *Int. J. Surg. Pathol.* 2014.22(1):12-32.

- [69] Yi F, Huang J, Yang L, et al. Automatic extraction of cell nuclei from H&E-stained histopathological samples. *J. Med. Imaging* 2017;4(2):027502.
- [70] Onder D, Zengin S, Sarioglu S. A Review on Color Normalization and Color Deconvolution Methods in Histopathology. *Appl. Immunohistochem. Mol. Morphol.* 2014;22(10):713-719.
- [71] Ruifrok A.C, Katz R.L, Johnston D.A. Comparison of Quantification of Histochemical Staining By Hue-Saturation-Intensity (HSI) Transformation and Color-Deconvolution. *Appl. Immunohistochem. Mol. Morphol.* 2003.11(1):85-91.
- [72] Macenko, M., Niethammer, M., Marron, *et al.* A method for normalizing histology slides for quantitative analysis 2009. 2009 IEEE International Symposium on Biomedical Imaging: From Nano to Micro:1107-1110.
- [73] Magee D, Treanor D, Crellin D, *et al.* Colour Normalisation in Digital Histopathology Images. The 12<sup>th</sup> International Conference on Medical Image Computing and Computer Assisted Intervention 2009:100-111.
- [74] Niethammer M, Borland D, Marron JS, *et al.* Appearance normalization of histology slides. In: Wang F, Yan P, Suzuki K, *et al.* Machine Learning in Medical Imaging Volume 6357 of Lecture Notes in Computer Science 2010. Berlin, Heidelberg. Springer:58–66.
- [75] Li S. A review of feature detection and match algorithms for localization and mapping. *IOP Conf. ser., Mater. Sci. Eng.* 2017.107;231:012003.
- [76] Lowe D.G. Object recognition from local scale-invariant features. *Proc. IEEE Int. Conf. Comput. Vis.* 1999.2:1150-1157.
- [77] Salahat E, Qasaimeh M. Recent advances in features extraction and description algorithms: A comprehensive survey. *IEEE International Conference on Industrial Technology* 2017.1059-1063.
- [78] Van der Walt S, Schönberger J.L, Nunez-Iglesias J, *et al.* Scikit-image: Image processing in Python. *PeerJ* 2014;2:453.

## **Chapter II: Development of Patient-Specific 3D Models from Histopathological Samples for Investigations in Radiation Therapy**

### **II.1 INTRODUCTION**

The biological effect of ionizing irradiation on living tissues is typically quantified through the physical quantity of absorbed dose. While absorbed dose is correlated with biological outcomes it does not uniquely determine the biological effectiveness of an irradiation. In radiation therapy, knowledge of cancer pathology, local oxygenation, radiation quality, and numerous other factors are required to determine the relationship between absorbed dose and a biological outcome such as tumor control probability [1-2]. An area of emerging interest is developing a greater understanding of the influence of the microscopic morphology of cells and nuclei on treatment outcomes in radiation therapy [3-5]. The development and increasing use of radiopharmaceutical therapy (RPT) has played a role in motivating such investigations. As ionizing radiation emitted by radioisotopes used in theragnostics have ranges in tissue varying from nanometers (Meitner-Auger emitters such as  $^{123}\text{I}$ ) up to centimeters (beta emitters such as  $^{90}\text{Y}$ ), knowledge of tissue morphology is needed to determine the microscopic distribution of energy depositions, which influences the biological effectiveness of the treatment [6-9]. Additionally, in external beam radiation therapy (EBRT) and brachytherapy, it has been demonstrated that target size impacts microscopic descriptors of energy deposition, such as lineal energy, which is the microscopic quantity corresponding to the linear energy transfer [10-11]. Currently, when determining microdosimetric quantities with Monte Carlo (MC) methods, target geometries of single sized spheres, ellipsoids, boxes or cylinders are used to mimic individual cells and nuclei [4, 12]. Some authors use a two-compartment model involving a smaller volume that is placed within the cell body representing a nucleus [5]. Whilst uniformly sized target geometries may provide useful

information for many cases, any effects that a cell/nucleus population with a range of volume sizes may have on the studied quantities is ignored.

Knowledge of a patient's cell, nucleus size, and morphology can be a necessary step in calculation of more accurate microdosimetric quantities that when combined with appropriate radiobiological models can be incorporated into future clinical treatment planning systems for patient-specific radiation therapy treatment planning.

Hematoxylin and eosin (H&E) are the most common stains used to generate contrast on histopathological samples [13]. H&E stained samples derive their contrast from their two constituent stains: Hematoxylin which is taken up by the nuclei of cells, staining RNA, DNA, and some extranuclear components purple or blue. Structures stained pink or red by eosin include the cytoplasm, numerous proteins, and connective structures [14]. H&E stained samples are already gathered as part of current clinical practice to diagnose most cancers and for research purposes can be processed in large volumes by being embedded in paraffin wax alongside other samples in a structure known as a tissue microarray (TMA). Given that H&E stained histopathological samples are already collected during clinical practice and reveal information about cells and nuclei they are an appropriate and widely available source of patient-specific information regarding cell spacing and nucleus size. With computational image analysis techniques, the local hematoxylin maxima corresponding to the location of a nucleus center can be automatically determined. The spacing between adjacent nuclei can be used to infer cell spacing, and the quantity of hematoxylin stained pixels present in each cell can yield a descriptor of the nucleus size.

While 3D information is not inherently present in two-dimensional (2D) histopathological samples, cell and nucleus size information has been used by Poole *et al.* (2015) to develop digital 3D models containing volumes of equivalent size to those found in a 2D histopathological sample

immunostained for HER-2 [15]. The existing methods developed by Poole *et al.* are not integrable with current clinical practice for most patients receiving radiation therapy as many histopathological samples are not positive for and thus will not show contrast when immunostained for HER-2. Additionally, the previous work has not determined the statistical uncertainties associated with the size extraction algorithm employed or quantified the packing fraction of the 3D models developed.

For a digital 3D model to be representative of a tissue sample, it should contain cell volumes with the same 3D packing fraction as the tissue sample it is derived from. Digital 3D models yielded from spherical pouring simulations, where volumes are dropped under the force of gravity into a volume and experience frictional and interaction forces are known to adopt packing fractions between the random loose packed and random close packed limits of approximately 55% and 64% respectively, for single sized volumes [16]. The extracellular volume fraction of cancerous tissues can be quantified *in vivo* using magnetic resonance imaging. Kim *et al.* (2004) measured a mean extracellular volume fraction of 36% in the center of a PCa 2b tumour model in a mouse (which corresponds to a mean cellular packing fraction of 64%) [17]. This finding suggests that digital models developed by pouring simulations may have packing fractions approximately equivalent to those found in live cancerous tissues.

## **II.II Aims**

In this work, methods are presented to extract cell spacing and nucleus radius distributions from digital images of H&E stained histopathological samples comparable to those taken as part of current clinical practice. A process to generate digital 3D models containing spherical cells and nuclei of sizes corresponding to those present in a histopathological sample, with a packing

fraction approximating live cancerous tissues is presented. The digital 3D models developed have applications in cellular dosimetry and microdosimetric studies.

## II.III. METHODS

### II.III.I Extraction of Cell and Nucleus Size Distributions from H&E Stained Samples

Sixty histological samples which had been extracted from lung adenocarcinoma patients using a TMA platform were considered for inclusion in the study. Each histopathological sample was stained with H&E. The thickness of each sample was  $5 \mu m$ . Digital images of the samples were acquired of size  $1.88 mm \times 1.88 mm$  with a resolution of  $4 \frac{pixels}{\mu m}$ . The samples were similar to those extracted as part of standard clinical practice, however were embedded in a TMA for bulk analysis. Exclusion criterion for further analysis are described in Table 2-1. Nineteen samples met the criteria for inclusion in the study.

Cell spacing and nucleus radius distributions were extracted from each sample. The location of each nucleus in the image was determined using a difference of gaussian (DoG) detection algorithm implemented in Scikit-Image [18]. A Delaunay triangulation was computed given the nuclei locations [19]. The distribution of Delaunay edge lengths divided by two gives the cell spacing distribution which is an analogue of cell radius.

An automatic thresholding algorithm was used to determine the nucleus radius distribution in a sample. The local minima in the red colour channel of the image between the peak corresponding to stain and the white background peak was determined. Background rejection was achieved by masking all pixels with an intensity value greater than the local minima in the red color channel.

**Table 2-1:** Exclusion criteria for H&E stained samples in the study.

<i>Criterion #:</i>	<i>Criteria</i>	<i>Justification</i>
1	Whitespace made up greater than 25% of the image surface area (not including background outside of sample).	Cell spacing is determined by distance between adjacent cells. Whitespace present in image artificially inflates measured cell spacing.
2	Image contained greater than 10% red blood cells by image surface area.	Information regarding the non-tumoral and cancerous cells present in a sample are desired. Blood cells move through the vascular system and are not typically considered the target for radiation therapy of solid tumours.
3	Contained fewer than 100 non-tumoral or cancerous cells.	The statistical uncertainties of both cell spacing and nucleus radius become unacceptably large. Also, the cell spacing algorithm can not properly quantify cell spacing when there are extremely few adjacent cells.

Determination of which pixels are hematoxylin dominant (stain deconvolution) is done by iterating over each pixel. If a pixel's red channel value was greater than its blue channel value, it was deemed to likely contain eosin rather than hematoxylin and was masked out. A circle of equivalent radius to the cell spacing previously determined was superimposed over the center of each nucleus identified. The hematoxylin dominant pixels present in each cell spacing circle were summed to determine how much nuclear content was associated with each cell. The nucleus area associated with each cell was converted to a radius assuming a spherical structure of the nucleus. The cell and nucleus segmentations were scrutinized under visual examination by a pathologist to ensure

correct operation of the algorithm. Cancerous and non-tumoral regions in each sample were contoured manually by a pathologist (Torres J.) such that separate cell spacing and nucleus radius distributions could be extracted for the non-tumoral and cancerous cells present in each image. A two-sided t-test comparing non-tumoral and cancerous cell and nucleus size distributions in the same histopathological sample was conducted.

### II.III.II Correction of Cell and Nucleus Size Distributions

The cell spacing and nucleus radius distributions determined were corrected to account for the presence of cells and nuclei which are cut during histological sample preparation. Cells and nuclei near the boundaries of a sample may be cut and appear with an apparent radius lesser than their true radius. Assuming that all cells and nuclei are spherical, and their positions are randomly distributed along the axial axis of the sample, one can analytically determine a point spread function (PSF) which describes how cells/nuclei of a given radius spread into other apparent radii in the image. The PSF is given by:

$$PSF = \frac{d}{d(r_{app})} \left[ \frac{rT}{r^2 \left( \frac{2-\pi}{4} \right) + rT} \left( r \cdot r_{app} - \frac{r^2 \cdot \arcsin\left(\frac{r_{app}}{r}\right)}{2} - \frac{r_{app} \sqrt{r^2 - r_{app}^2}}{2} \right) \right] \quad (2 - 1)$$

Where  $r$ , refers to the true radius of the cell/nucleus,  $T$  the axial thickness of the histology slide,  $r_{app}$  the apparent radius which the cell/nucleus may appear as in the slide, and  $d$  is the differential operator in Leibniz notation. An optimization problem was posed, in which the cell/nucleus size distributions were decomposed into a summation of PSFs. The decomposition was accomplished using a non-negative least squares optimization [20]. The coefficient associated with each PSF yields the best guess for the true number of cells/nuclei of a given radius present in the slide.

### **II.III.III Generation of Representative Three-Dimensional Tissue Models**

A cell spacing distribution derived from a cancerous region of an H&E stained slide was sampled to populate the diameter of hard spheres in a Large-scale Atomic/Molecular Massively Parallel Simulator (LAMMPS) pouring simulation [21]. Spheres whose diameters correspond to patient-specific cellular spacing lengths are poured into a cube of 250  $\mu\text{m}$  side length. Spheres at the sides of the box experience periodic boundary conditions meaning they experience forces from spheres present on the opposite side of the box. Spheres at the top and bottom of the box (parallel with the direction of gravity) are subjected to a hard boundary. Interactions between spheres are modelled using a Hookean force model with large force constants to ensure the poured cells behave as hard spheres. After development of the 3D cellular model the distribution of nucleus radii is sampled to fill each cell with an appropriately sized nucleus. A correction to the nucleus radius distribution was applied to correct for the situation in which a nucleus sphere is sampled from the distribution which is larger than the cell sphere into which it is intended to be placed. The correction ensures that the 3D model generated does not bias towards small nuclei. The correlation between cell and nucleus radius was not investigated in this work as the number of cells present in a single sample is too few to determine a relationship between cell and nucleus size with appropriate statistical uncertainties.

## **II.IV. RESULTS**

A representative histopathological sample on which analysis was performed is shown along with histograms of its red, green, and blue color channels (Figure 2-1). Peaks corresponding to white background pixels were observed at intensity values greater than 240 in each color channel. A cropped region of a representative sample is shown (Figure 2-2). The resultant cell segmentation yielded by a DoG algorithm is depicted on the same cropped region, with cell centroids shown as

black dots and circles of equivalent cell spacing distance superimposed. The result yielded by the stain deconvolution algorithm is demonstrated on the cropped image which contains only pixels that were thought to be hematoxylin dominant.

The cell spacing and nuclei radius distributions of all slides analyzed are summarized in a box and whiskers plot (Figure 2-3). A median cell spacing of  $7.3 \mu\text{m}$  and  $8.2 \mu\text{m}$  and was observed in non-tumoral and cancerous regions respectively. A median nucleus radius of  $3.1 \mu\text{m}$  and  $4.0 \mu\text{m}$  was observed in non-tumoral and cancerous regions. The mean cell spacing and nucleus radius was greater for cancerous than non-tumoral regions in 18 of 19 samples studied. All non-tumoral nucleus radius distributions were significantly different ( $p < 0.01$ ) from cancerous nucleus radius distributions in the same sample, and 18 of 19 cell spacing distributions showed significant differences between non-tumoral and cancerous cell spacing distributions determined from the same sample ( $p < 0.01$ ). The average nuclear-cytoplasmic ratio (NCR) of non-tumoral regions was 0.36 while a value of 0.5 was observed in cancerous regions (Figure 2-4). A rendering of a LAMMPS pouring simulation in progress is shown (Figure 2-5). Developed 3D models were encoded in plaintext files, with the coordinates and radius of each spherical volume on a separate line. The packing density of 100 generated 3D models was 65.9% (SD: 1.5%) and 13.3% (SD: 0.3%) for cells and nuclei respectively (Figure 2-6).

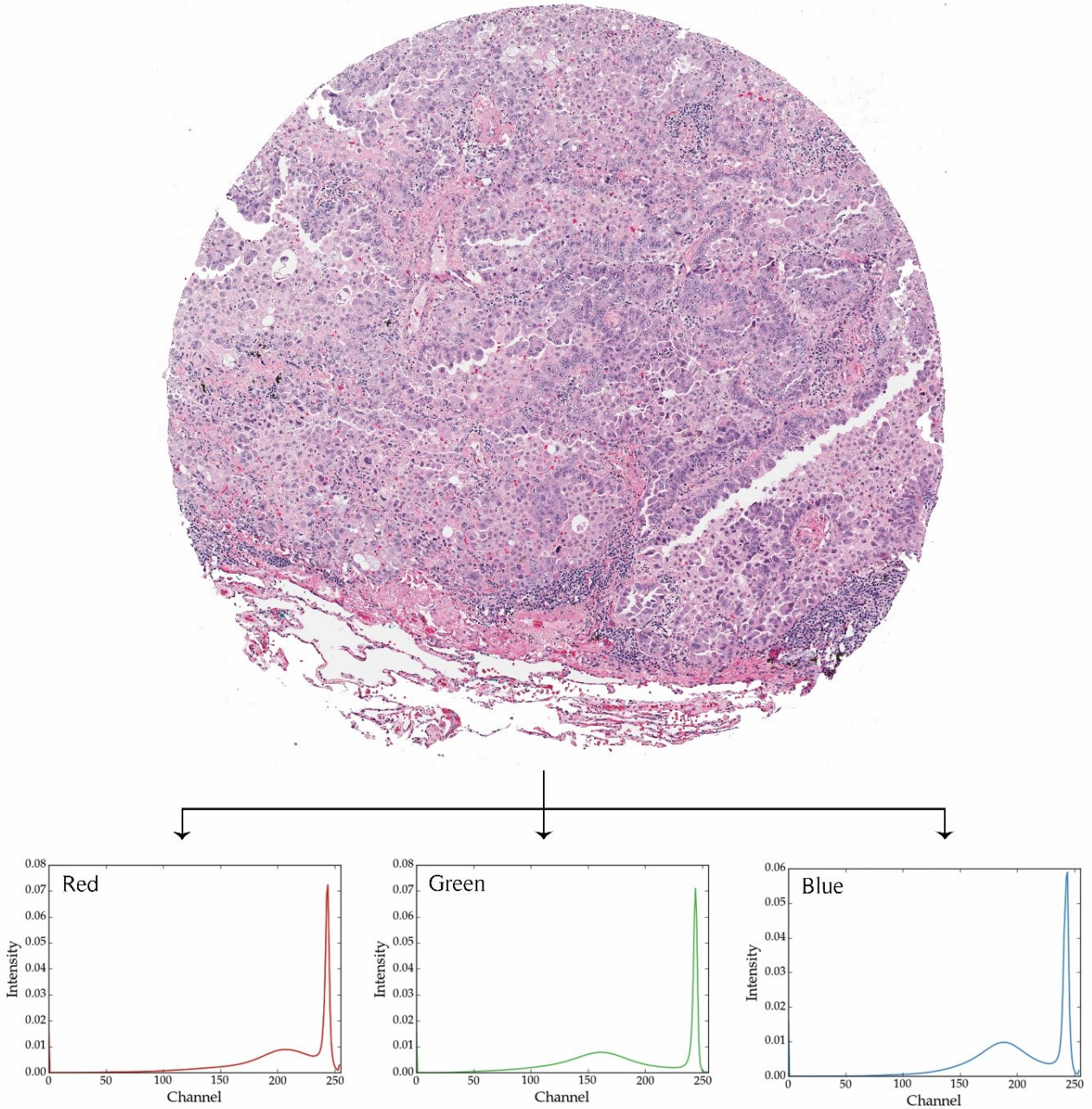


**Figure 2-1:** (top) Representative H&E stained pathology sample of lung adenocarcinoma. (bottom) Histogram of image intensity in the red, green, and blue colour channels respectively.

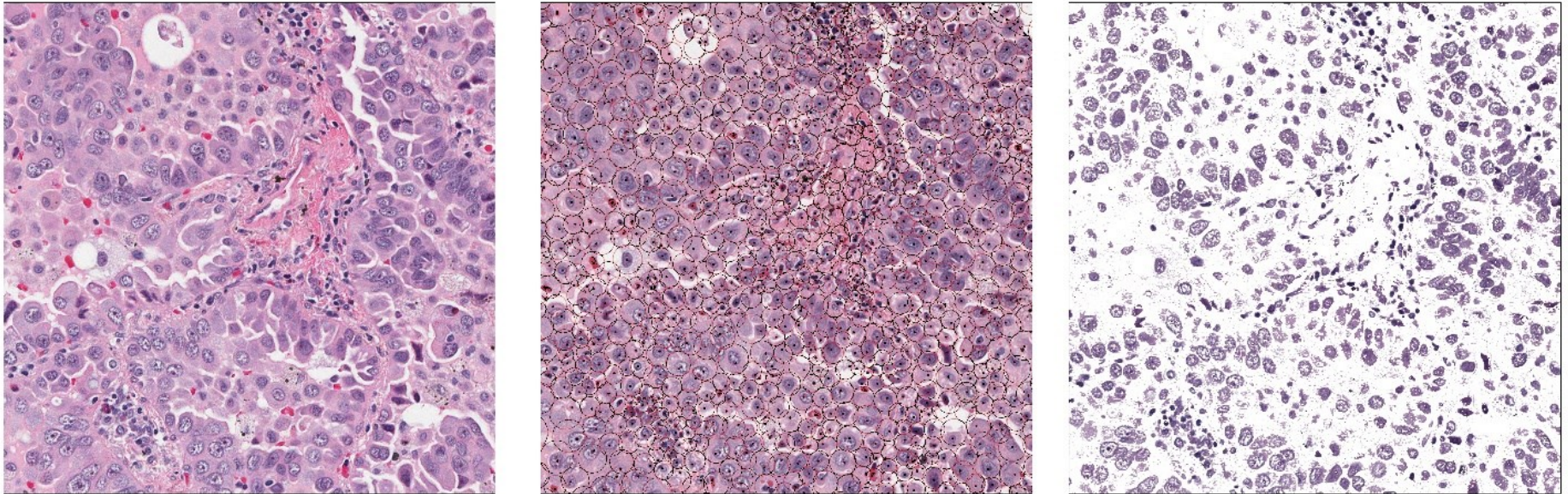


**Figure 2-2:** (Left) Magnified region of a representative H&E stained sample. (Center) The centroid of each cell identified by the DoG algorithm and circle of equivalent cell spacing area is superimposed on the slide. (Right) Resultant image after thresholding is applied to extract Hematoxylin dominant regions.

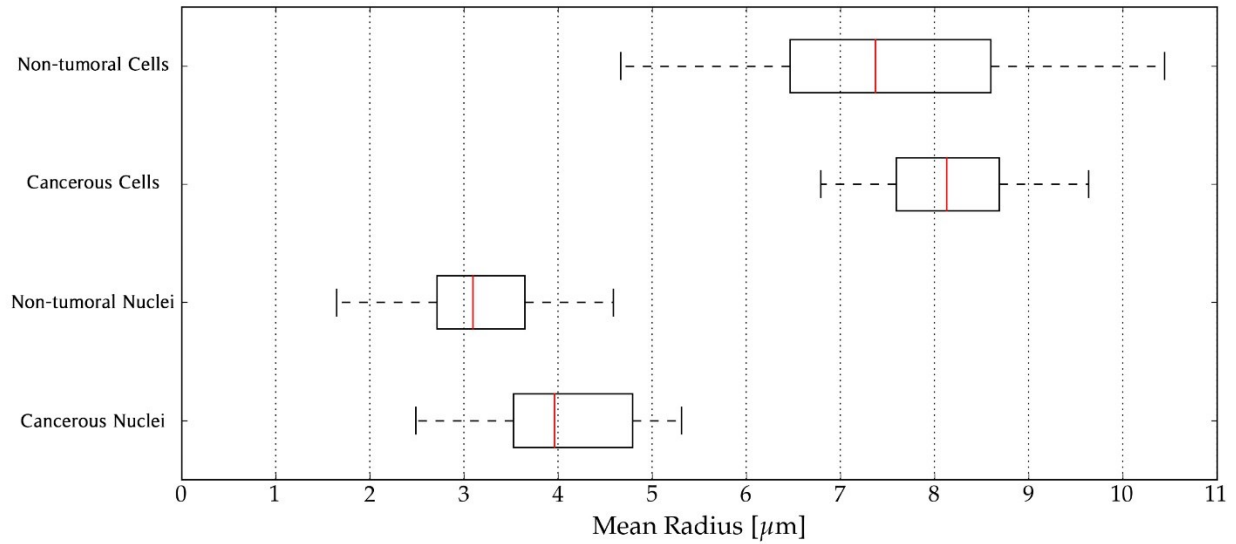


**Figure 2-3:** Mean cell spacing radius and nucleus radius of the 19 slides analyzed. Red lines in the center of boxes identify the median, boxes represent quartiles, and whiskers identify minima and maxima.

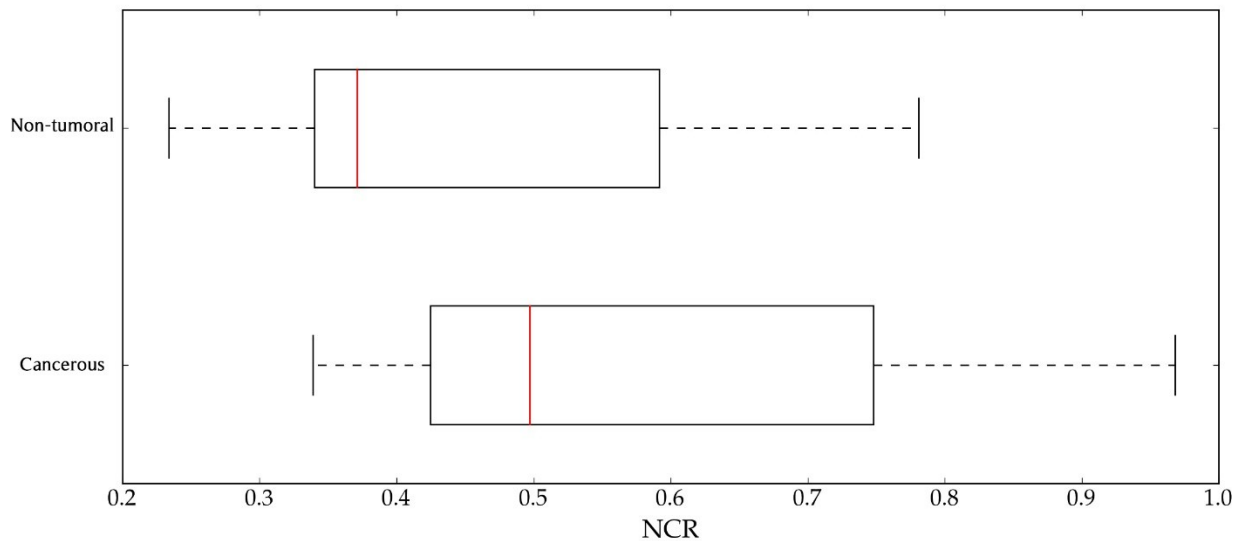


**Figure 2-4:** Mean NCR in the 19 slides analyzed stratified by non-tumoral and cancerous regions. Red lines in the center of boxes identify the median, boxes represent quartiles, and whiskers identify minima and maxima.

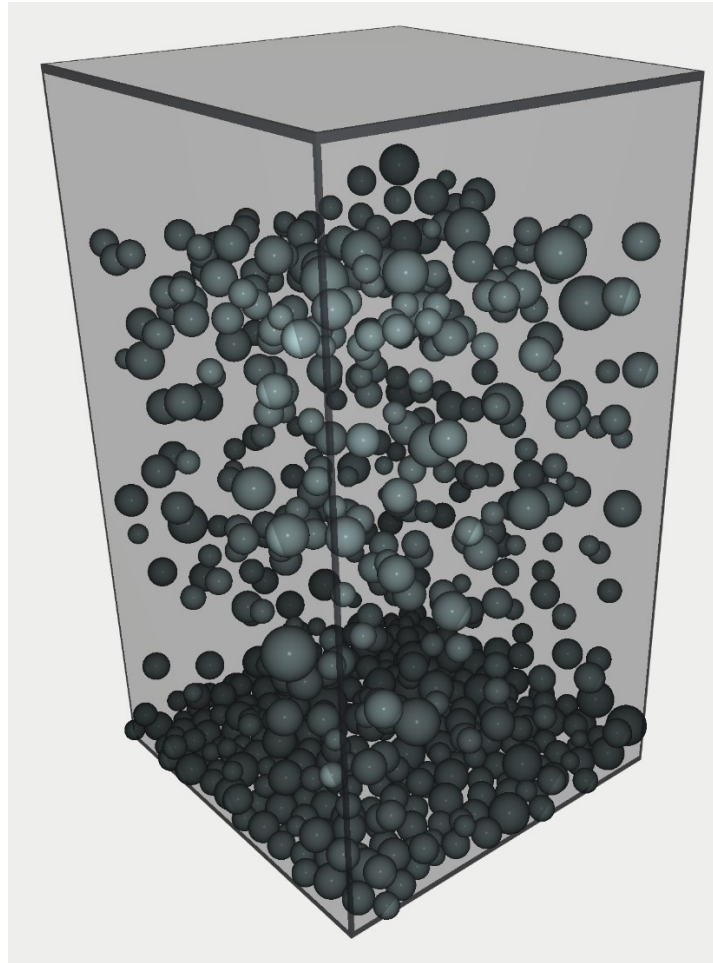


**Figure 2-5:** Rendering of a pouring simulation in progress generated using Atomify LAMMPS. The radius of spherical volumes is sampled from a cancerous cell spacing radius distribution.

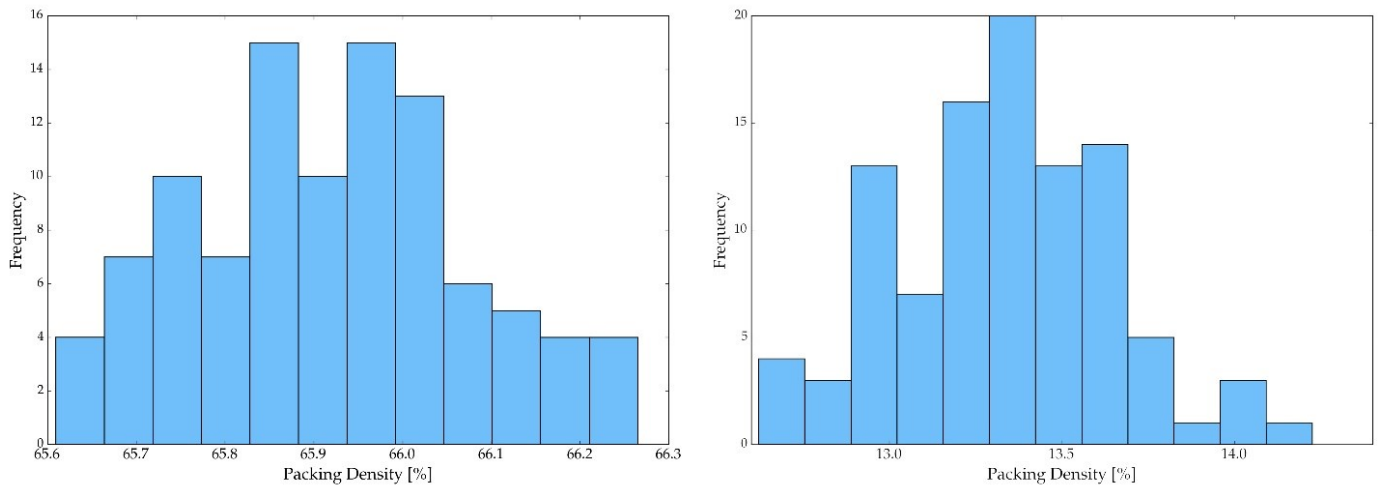


**Figure 2-6:** Packing density histogram of 100 generated 3D models (Left) Cellular density (Right) Nucleus density.

## II.V. DISCUSSION

### II.V.I Extraction of Cell and Nucleus Size Distributions from H&E Stained Samples

A method is presented for automated extraction of cell spacing and nucleus radius distributions from digital histopathological samples comparable to those taken as part of current clinical practice. One expects to observe distinct cell spacing and nucleus radius distributions in non-tumoral and adjacent cancerous regions for several reasons. In non-tumoral tissue, the size of cells and nuclei depends primarily on the tissue type and cell cycle. While, in cancerous tissue, and especially in solid tumors, chromosomal instability leads to greater variability in size and shape of the nucleus. The difference in nuclear size (anisokaryosis), shape, and chromatin patterns of cancerous tissues all effect the size distributions determined from histopathological samples. Commonly, the nuclei of tumoral cells appear larger and darker (hyperchromatism), with a greater NCR than that of adjacent non-tumoral cell nuclei due to an excess of DNA content within its volume [22]. The methods used in this study were sensitive to the differing cell spacing and nucleus radius distributions of non-tumoral and cancerous tissues. The median NCR of cancerous regions was found to be 14% greater than non-tumoral regions studied and a statistically significant difference in nucleus radius distributions of nuclei in non-tumoral and cancerous regions of a sample was found.

An important caveat to our measurements of NCR is that the segmentation method used does not provide information about the extent of the cell membrane. The cell spacing then determined by our segmentation algorithm represents the space between two adjacent nuclei, which is the algebraic sum of the cell size and extracellular space. It has been widely reported that the extracellular matrix (ECM) is disturbed between cancerous cells which can include decreased

matrix density [23]. If this understanding is correct, the observed NCR between non-tumoral and cancerous cells may be increasing to a greater extent than our findings indicate.

## **II.V.II Potential Improvements to Accuracy of Developed Tissue Models**

Which cell populations are most responsible for the dose response of ionizing radiation remains to be determined. In cancerous tissues, there exists a mixture of cancerous cells with non-tumoral cells including: stromal, immune, and vascular cells. Non-tumoral cells are thought to have an important role in tumor growth and disease progression [24]. Therefore, it may be more appropriate to develop 3D tissue models with volumes which span the range of radii present in an entire histopathological sample rather than to develop distinct 3D models for non-tumoral and cancerous regions of a sample.

A two-step thresholding approach was used to perform background rejection and stain deconvolution on the samples we studied (i.e. to separate hematoxylin dominant pixels from eosin dominant pixels). Our stain deconvolution method assumes that a flat plane in RGB space exists which distinguishes hematoxylin from eosin dominant pixels, while evidence suggests that the distinguishing surface is more accurately described by a curve in RGB space [25]. Certainly, other stain deconvolution methods which have been developed may be substituted into the workflow presented in our study to more accurately determine nucleus radius distributions. Fortunately, some of the erroneous hematoxylin dominant regions which appear as noise outside of the nucleus may not be contained within a cell spacing circle and thus are ignored in the calculation of the nucleus radius (Figure 2-2). The method of stain deconvolution employed in our study was chosen because of its relative computational simplicity compared to other methods [26]. For the same reasons, a DoG blob detection technique was used rather than the more computationally demanding Laplacian of Gaussian algorithm, or machine learning based approaches seen in many

recent studies of cell and nucleus segmentation [27]. Computational efficiency in the workflow presented in our study was desired such that the methods presented are accessible to as wide a community as possible, including researchers and those who may desire to integrate 3D patient-specific tissue models into a clinical treatment planning system. The entire workflow presented in this study, including H&E stained sample analysis and development of a corresponding 3D model can be conducted in less than an hour on a single core of a 6th generation Intel desktop processor.

A source of inaccuracy in the current cell and nucleus size determination method involves the conventional microscopy techniques used in histopathological imaging. 3D information about a cell is neglected with conventional microscopy and the size of a cell or nucleus is inferred by an arbitrary 2D projection of the object. If confocal microscopy were used to image the histopathological samples one could acquire 3D information about the objects appearing in the slide. This could allow cells and nuclei to be modelled as a tri-axial ellipsoid with three differing axis lengths. Confocal microscopy imaging is not a part of current clinical practice at the institution where samples were acquired and thus was not investigated. Additionally, the force models of the pouring simulations used would have to be modified in order simulate ellipsoidal rather than spherical volumes.

The mean cellular packing density of 3D tissue models we developed using a pouring simulation was found to be within 2% of the mean packing density of a tumour as measured *in vivo* by Kim *et al.* using MRI [17]. The extracellular volume fraction is known to vary spatially throughout a tumour, which suggests that characterization of the cellular packing density of a cancer type by a single quantity may not be appropriate [28]. If the extent of the cell membrane were determined using the eosin stained components of an H&E stained sample, a patient-specific packing density could be extracted from the histopathological samples used in this study. The packing density of

poured models are known to be dependent on the shape of ellipsoidal grains and the friction between such grains [29]. If cells were modeled as tri-axial ellipsoids as previously described, the packing density of the developed model may naturally approach the packing density of the tissue from which the model is developed. If not, a method to vary the frictional parameters of a pouring simulation may be used to generate a 3D model with a packing density which matches the cellular packing density observed in a histopathological sample.

### **II.V.III Applications of Tissue Models**

The potential applications of the models presented in this work are broad and not limited to any particular source of ionizing radiation, to determination of any particular quantity, and perhaps not even to radiation therapy.

Recent interest has been expressed in using accurate cell and nucleus models for the determination of S-values of theragnostics [3]. Particularly for theragnostics which rely on the emission of Meitner-Auger electrons or alpha particles for tumour ablation, one expects extreme microscopic variability in energy deposition between biological volumes of interest [7-9,30-31]. This variation occurs because of the relatively low number of tracks one expects will deposit energy in any given target, owing to the short track lengths of Meitner-Auger electrons and alpha particles. Knowledge of the size and spacing between a population of cells will influence a quantity known as the cross S-value, the mean absorbed dose deposited in a volume from a radionuclide which decayed in another nearby volume [30]. As existing calculations of cross S-values are frequently computed in models of single sized volumes placed in a simple grid, the models developed here allow for a more accurate computation of cross S-values than existing methods.

In addition to computation of S-values for RPT, the models developed in this study have applications in EBRT and brachytherapy. Values in microdosimetry, including specific energy are known to be strongly dependent on target size [4,11]. Variation in specific energy deposited between biologically sensitive volumes including the cell nucleus impacts the biological effectiveness of a treatment. Radiobiological models such as the microdosimetric kinetic and local effect model can predict the biological effectiveness of a radiation therapy treatment given knowledge of energy deposition from ionizing radiation in nucleus sized volumes [32-33]. Investigation of energy depositions in 3D tissue models may allow for patient-specific modelling of dose response and enhance prognostic abilities in radiation therapy when paired with a radiobiological model.

## II.VI CONCLUSIONS

Methods to extract cell and nucleus size information from H&E stained histopathological samples commonly extracted as part of current clinical practice are shown. 3D models with cell and nucleus volumes of equivalent radius to those extracted from a cancerous region of an H&E stained histopathological sample are then developed. 3D digital tissue models are developed through pouring simulations which include an arrangement of volumes that approximates the cellular packing fraction of some cancerous tissues. Potential applications of these tissue models exist in cellular dosimetry and microdosimetry for EBRT, brachytherapy, and RPT.

## References

- [1] Hall E.J, Giaccia A.J. Radiobiology for the Radiologist 7<sup>th</sup> ed. Philadelphia PA: Lippincott Williams & Wilkins (2012).
- [2] Stewart R.D, Carlson D.J, Butkus M.P, et al. A comparison of mechanism-inspired models for particle relative biological effectiveness (RBE). *Med. Phys.* 2018.45(11):e925-e952.

- [3] Tamborino G, Saint-Hubert M.D, Struelens L, et al. Cellular dosimetry of [<sup>177</sup>Lu]Lu-DOTA-[Tyr<sup>3</sup>]octreotate radionuclide therapy: the impact of modeling assumptions on the correlation with in vitro cytotoxicity. *Eur. J. Nucl. Med. Mol. I. Phys.* 2020;7(8).
- [4] Villegas F, Tilly N, Ahnesjö A. Microdosimetric spread for cell-sized targets exposed to Co-60, Ir-192 and I-125 sources. *Radiat. Prot. Dosim.* 2015;166(1-4):365-368.
- [5] Oliver P.A.K, Thomson R.M. Investigating energy deposition within cell populations using Monte Carlo simulations. *Phys. Med. Biol.* 2018;63(15).
- [6] Meitner, L. Über die Entstehung der  $\beta$ -Strahl-Spektren radioaktiver Substanzen. *Z. Physik* 1922;9:131–144.
- [7] Cornelissen B, Vallis K.A. Targeting the Nucleus: An Overview of Auger-Electron Radionuclide Therapy. *Curr. Drug Discov. Technol.* 2010;7.
- [8] Hofmann W, Li W.B, Friedland W, et al. Internal microdosimetry of alpha-emitting radionuclides. *Radiat. Environ. Biophys.* 2020;59:29–62.
- [9] Bavelaar B.M, Lee B.Q, Gill M.R, et al. Subcellular Targeting of Theranostic Radionuclides. *Front. Pharmacol.* 2018;9:996.
- [10] Lindborg L, Hultqvist M, Carlsson Tedgren Å, et al. Lineal energy and radiation quality in radiation therapy: model calculations and comparison with experiment. *Phys. Med. Biol.* 2013;58:3089-3105.
- [11] Famulari G, Pater P, Enger S.A. Microdosimetric Evaluation of Current and Alternative Brachytherapy Sources – A Geant4-DNA Simulation Study. *Int. J. Radiat. Oncol. Biol. Phys.* 2017;100(1):270-277.
- [12] Mori R, Matsuya Y, Yoshii Y, et al. Estimation of the radiation-induced DNA double-strand breaks number by considering cell cycle and absorbed dose per cell nucleus. *Radiat. Res.* 2018;59(3):253-260.
- [13] Kleczek P, Jaworek-Korjakowska J, Gorgon M. A novel method for tissue segmentation in high-resolution H&E-stained histopathological whole-slide images. *Comput. Med. Imag. Grap.* 2020;79:101686.
- [14] Bancroft, J.D., Layton, C. The hematoxylin and eosin. In: Suvarna, S.K., Layton, C., Bancroft, J.D. Bancroft's theory and practice of histological techniques, 7th Edition. Churchill Livingstone:173–186(2013).
- [15] Poole C.M, Ahnesjö A, Enger S.A. Determination of subcellular compartment sizes for estimating dose variations in radiotherapy. *Radiat. Prot. Dosim.* 2015;166(1-4):361-364.
- [16] Song C, Wang P, Makse H.A. A phase diagram for jammed matter. *Nature* 2008.453;629-632.
- [17] Kim Y.R, Savellano M.D, Savellano R, et al. Measurement of Tumor Interstitial Volume Fraction: Method and Implication for Drug Delivery. *Magn. Reson. Med.* 2004;52:485-494.
- [18] Van der Walt S, Schönberger J.L, Nunez-Iglesias J, et al. Scikit-image: Image processing in Python. *PeerJ* 2014;2:453.

- [19] Vu Q.D, Garham S, Kurc T, *et al.* Methods for Segmentation and Classification of Digital Microscopy Tissue Images. *Front. Bioeng. Biotechnol.* 2019;7(53).
- [20] Lawson C.L, Hanson R.J. Solving Least Squares Problems. Philadelphia, USA, Society for Industrial and Applied Mathematics, 1987.
- [21] S. Plimpton. Fast Parallel Algorithms for Short-Range Molecular Dynamics. *J. Comp. Phys.* 1995;117:1-19.
- [22] Baba A.I, Cătoi C. Comparative Oncology. Bucharest, Romania, The Publishing House of the Romanian Academy, 2007.
- [23] Aro E, Salo A.M, Khatri R, *et al.* Severe Extracellular Matrix Abnormalities and Chondrodysplasia in Mice Lacking Collagen Prolyl 4-Hydroxylase Isoenzyme II in Combination with a Reduced Amount of Isoenzyme. *J. Biol. Chem.* 2015;290(27):16964-16978.
- [24] V Kumar, A K Abbas and J C Aster (Eds.). *Robbins basic pathology* (9th ed.). Philadelphia, PA: Elsevier Saunders (2013).
- [25] Macenko, M., Niethammer, M., Marron, J.S, *et al.* A method for normalizing histology slides for quantitative analysis. 2009 IEEE International Symposium on Biomedical Imaging: From Nano to Macro, 1107–1110.
- [26] Ruifrok A.C, Johnston D.A. Quantification of histochemical staining by color deconvolution. *Anal. and Quant. Cyto. Hist.* 2001.23:291-299.
- [27] Xing F, Yang L. Robust Nucleus/Cell Detection and Segmentation in Digital Pathology and Microscopy Images: A Comprehensive Review. *IEEE Rev. Biomed. Eng.* 2016;9:234-263.
- [28] Arlinghaus L.R, Li X, Rahman A.R, *et al.* On the relationship between the apparent diffusion coefficient and extravascular extracellular volume fraction in human breast cancer. *Magn. Reson. Med.* 2011;29:630-638.
- [29] Delaney G.W, Hilton J.E, Cleary P.W. Defining random loose packing for nonspherical grains. *Phys. Rev. E* 2011.83:051305-1.
- [30] Enger S.A, Hartman T, Carlsson J *et al.* Cross-fire doses from beta-emitting radionuclides in targeted radiotherapy: A theoretical study based on experimentally measured tumor characteristics. *Phys. Med. Biol.* 2008;53(7):1909-1920.
- [31] Josefsson A, Forssell-Aronsson E. Microdosimetric analysis of I-123, I-125 and I-131 in thyroid (follicle) models. *Jour. Nuc. Med.* 2013;54(2).
- [32] Hawkins R.B. A microdosimetric-kinetic model of cell death from exposure to ionizing radiation of any LET, with experimental and clinical applications. *Int. J. Radiat. Biol.* 1996;69(6):739-755.
- [33] Friedrich T, Scholz U, Elsasser T, *et al.* Calculation of the biological effects of ion beams based on the microscopic spatial damage distribution pattern. *Int. J. Radiat. Biol.* 2012;88(1-2):103-107.

## Chapter III: Patient-Specific Microdosimetry

### III.I INTRODUCTION

Microdosimetry involves the study of the random nature of energy deposition from single tracks of ionizing radiation, typically with the aim of better understanding the biological effect of an irradiation on living tissues. Macroscopic quantities, such as absorbed dose,  $D$ , are in fact expectation values of other quantities which are randomly distributed on the microscopic level [1]. The microscopic quantity corresponding to dose is specific energy,  $z$ . For a patient receiving a dose of ionizing radiation, one expects there will be some variation in the specific energy deposited in microscopic targets such as cells or nuclei, not because of any limitation of the treatment delivery, but simply due to the stochastic nature of energy deposition by ionizing radiation.

A value of interest in microdosimetry is lineal energy,  $y$ . Much like specific energy is the microscopic analog of absorbed dose, lineal energy is the microscopic analog of linear energy transfer (LET). Lineal energy and LET are both physical parameters which through modelling can give an indication of the yield of biological damage for a given absorbed dose of ionizing radiation (i.e. the biological effectiveness of an irradiation). Lineal energy is defined as the quotient of total energy imparted to a volume,  $d\varepsilon$ , and the mean chord length through that volume,  $L$ , giving  $y = \frac{d\varepsilon}{L}$  [2]. LET is defined as the average energy transfer by a track of ionizing radiation,  $dE$ , traversing a distance,  $dx$ , giving  $LET = \frac{dE}{dx}$ . LET is only of a function of radiation type, energy spectra, and the material which ionizing radiation is interacting with, while lineal energy statistically fluctuates between microscopic targets depending on the number and magnitude of energy deposition events which occur within a target. A strength of lineal energy is that it only characterizes energy which is imparted locally, while LET characterizes energy transferred, some of which is transferred to

particles with sufficient energy to travel non-negligible distances and deposit energy elsewhere. It is thought that the ability of lineal energy to characterize local energy deposition and to characterize variation in energy deposition between targets make it a more suitable physical parameter for modelling biological damage induced by ionizing radiation than LET [3].

Information in microdosimetry is typically represented by probability density functions (PDFs). PDFs used to describe lineal energy include  $f(y)$ , a function representing the probability density of a volume receiving an amount of lineal energy from a single track of ionizing radiation. A related function  $d(y)$ , characterizes the fractional amount of dose delivered to a volume by tracks of a given lineal energy. The mean values of each function are known as the frequency mean lineal energy ( $\bar{y}_f$ ) and dose mean lineal energy ( $\bar{y}_d$ ) respectively.

The relative biological effectiveness (RBE) refers to the ratio of absorbed dose from two different sources of radiation in order to achieve the same biological effect for a given endpoint.  $f(y)$  and  $d(y)$  are often investigated in order to characterize the RBE of a radiation quality [4]. Computational microdosimetry has often limited itself to determination of microdosimetric parameters in volumes of a single fixed radius, arranged in a geometric grid without any spacing. Recent work has demonstrated that microdosimetric parameters determined in models containing a distribution of sizes and not arranged in a geometric grid are meaningfully different than those determined in fixed radius volumes [5-6]. We believe that such microdosimetric distributions yield a more accurate representation of the microdosimetric distributions one would find in living tissues, where biological targets have a distribution of sizes and are not arranged in a geometric grid. It remains to be seen if  $f(y)$  determined in volumes of variable size and spacing yields a meaningfully different RBE when propagated through a radiobiological model compared to conventional fixed radius methods.

The calculation of  $f(y)$  using Monte Carlo methods in tissue models with targets of varying size and spacing is extremely computationally involved, requiring on the order of 1 core-year of processor time, this necessitates use of a supercomputing cluster. Given that cell and nucleus size distributions will depend on tissue type, cancer morphology, and stage it will be necessary to compute such microdosimetric parameters each time a patient-specific prediction of RBE is desired. Similarly, in tissue cultures irradiated during cell studies, knowledge of  $f(y)$  yields important information about radiosensitivity but will need to be calculated repeatedly for each cell line studied and as target size varies at different time points [7]. Development of techniques for determination of  $f(y)$  in tissue models will allow for a more robust quantitative understanding of the variation in dose response due to changes in morphology and size of cells and nuclei. The barriers to incorporating such methods into a research or clinical workflow will be greatly reduced if fast computational methods of tissue-specific microdosimetric parameters are developed.

### **III.II Aims**

In this work, fast methods to calculate microdosimetric parameters including  $f(y)$  and  $d(y)$  in targets of varying size and spacing are proposed and evaluated. A method to pair the fast methods with cell and nucleus size information extracted from histopathological samples is demonstrated, enabling patient-specific microdosimetry with the computational resources of a single personal computer. The radiobiological consequences (i.e. influence on RBE) of such patient-specific microdosimetric data remains to be investigated in future work.

### III.III METHODS

#### III.III.I Generation of Tissue Models from Histological Samples

A histopathological sample extracted from a stage I lung adenocarcinoma patient using a tissue microarray (TMA) platform was analyzed in the study (Figure 3-1). The histopathological sample was stained with haematoxylin which is selectively taken-up by the nuclei. The thickness of the histopathological sample was 5  $\mu\text{m}$ . A digital image of the histopathological sample was acquired of size 525  $\mu\text{m}$  x 700  $\mu\text{m}$  with a resolution of 2.3  $\frac{\text{pixels}}{\mu\text{m}}$ . The sample was extracted as part of a prior study to investigate a correlation between genomic content and patient ethnicity in lung adenocarcinoma [8].

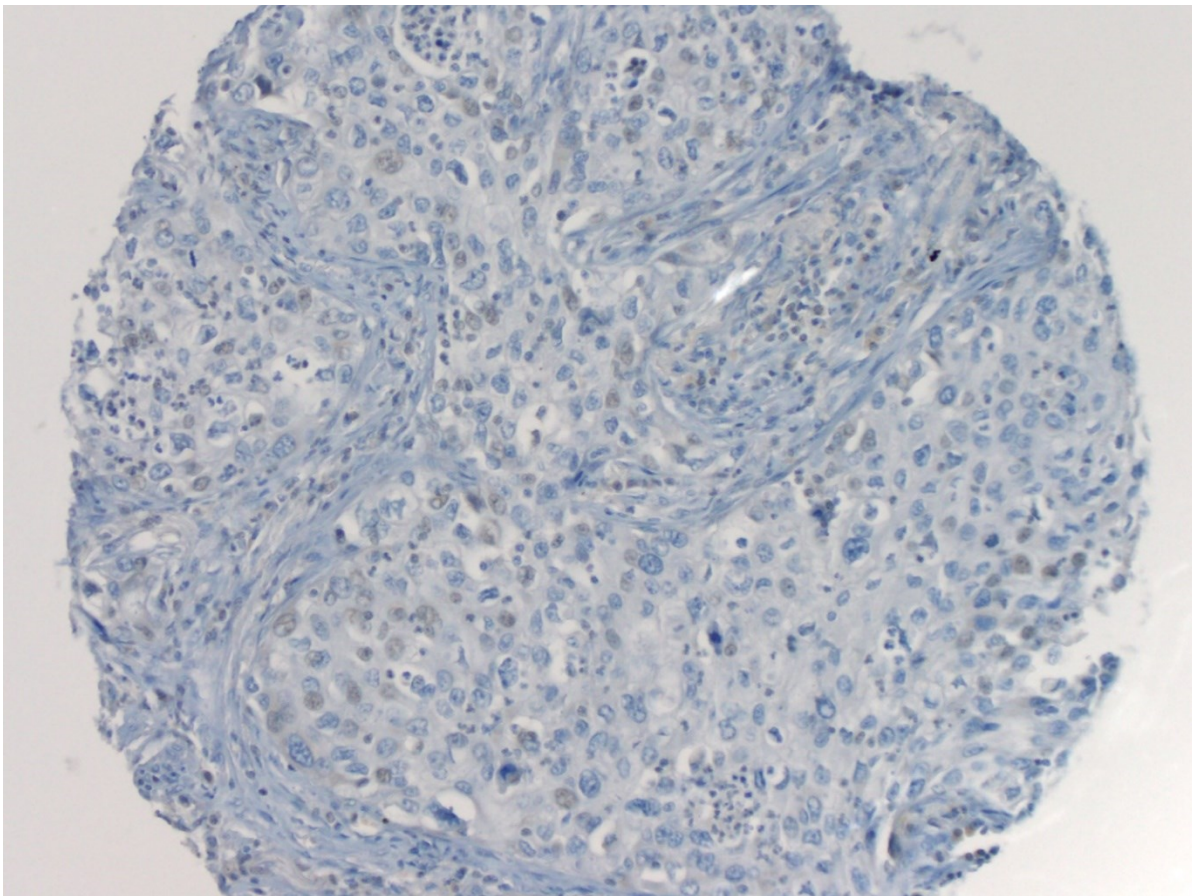


**Figure 3-1:** Digital image of a hematoxylin stained sample from a stage I lung adenocarcinoma patient, which was analyzed for determination of cancerous cell spacing and nucleus radius in our study.

Cell spacing and nucleus radius distributions were extracted from the sample studied using an automated algorithm suitable for use on hematoxylin or hematoxylin and eosin stained histopathological samples. The identification of cell centroids and determination of which pixels contained nucleus material were verified by visual inspection. The cell spacing and nucleus radius distributions extracted from the sample were corrected for cells and nuclei cut during histological sample preparation by use of a non-negative least squares optimization (NNLSO) based approach. A pouring simulation in which spheres of radii taken from the cell spacing distribution are dropped under the force of gravity and interact with each other through a hookean force model was used to develop a three-dimensional tissue model. Each cell spacing sized sphere had a spherical nucleus placed into it. The radius of each nucleus was randomly sampled from the nucleus radius distribution extracted from the sample. Material composition of cells and nuclei were modelled as water with unit density as no consensus on the elemental composition of tumor and healthy cells/nuclei exists [9]. The methods used for determination of cell spacing and nucleus radius distributions from histological samples as well as the development of digital 3D tissue models in this study are described in our other work and the reader is directed to that study for further information [10]. The stain present in the sample studied was different from those investigated in the prior study. The sample investigated in this work was stained with hematoxylin alone and thus requires no stain deconvolution as there is only a single stain present. The lower bound of the full-width half maximum of the haematoxylin peak in the blue color channel was used to distinguish stain containing pixels in the nucleus from non-nuclear regions.

### **III.III.II Monte Carlo Simulation**

Monte Carlo simulations were performed using the Geant4 radiation transport toolkit version 10.3 Patch 3 [11]. The radioactive decay photon spectra come from the Evaluated Nuclear Structure

Data File which is maintained by Brookhaven National Laboratory [12]. Electromagnetic interaction probabilities were determined using the Livermore condensed history cross sections. Computations were performed on the Niagara supercomputer on the SciNet HPC Consortium and the Beluga supercomputer of Calcul Québec [13].

### **III.III.II.I Determination of Electron Spectra**

Electron spectra were scored at a fixed radial distance of 1 cm from  $^{60}\text{Co}$ ,  $^{192}\text{Ir}$ , and  $^{169}\text{Yb}$  high dose rate brachytherapy sources encapsulated within a microSelectron v2 seed (Elekta Brachytherapy, Veenendaal, The Netherlands). The low dose rate brachytherapy source  $^{125}\text{I}$  was also simulated by use of a SelectSeed<sup>®</sup> (Elekta Brachytherapy, Veenendaal, The Netherlands) source model. The active core of the source was modified according to the selected radionuclide. The sources were placed at the center of a spherical water phantom of 1 m diameter.

Electron spectra were scored by recording the energy of any electron created in or colliding with a spherical shell of 1 cm radius and a thickness of 0.1 cm, centered about the source. The radius of the scoring shell was chosen to study the spectra of the source in the region which would contain the target during a treatment. The thickness of the scoring shell was chosen to be small enough that the photon spectra should not meaningfully change over its distance. Electrons were no longer tracked after their energy was recorded. A number of histories were run such that the average uncertainty in any bin of the spectra was less than 0.5% in 200 logarithmically spaced bins. The production and tracking cutoff for secondary particles was set to the lowest value at which the Livermore electromagnetic model is thought to be applicable, 25 eV.

### III.III.II.II Patient-Specific Microdosimetric Distributions

A patient-specific model derived from cancerous cell spacing and nucleus radius information referred to as the full model, was placed at the center of a water volume (Figure 3-2). To ensure charged particle equilibrium and prevent biasing, electron spectra were sampled throughout and around the model region in a cube larger than the model by the continuous slowing down approximation (CSDA) range of the highest energy electron in the spectra on all sides [14]. Energy imparted in nucleus volumes were recorded after a track had deposited all of its energy. Given the quantity of energy imparted to each volume from a single track, the lineal energy probability density,  $f(y)$  was calculated:

$$P(a < y < b) = \int_a^b f(y) \cdot dy \quad (3 - 1)$$

Where  $a$  and  $b$  are arbitrary constants and  $P$  is the absolute probability. The mean value of  $f(y)$ ,  $\bar{y}_f$  (frequency mean lineal energy) is calculated by the standard method for PDFs:

$$\bar{y}_f = \int_{-\infty}^{\infty} y \cdot f(y) \cdot dy \quad (3 - 2)$$

The fractional amount of dose deposited by tracks of a certain lineal energy,  $d(y)$  is then determined from  $f(y)$  by:

$$d(y) = \frac{y}{\bar{y}_f} f(y) \quad (3 - 3)$$

A variable number of tracks were simulated for each source such that each  $f(y)$  distribution contained  $10^5$  unique energy depositions. Uncertainty in  $f(y)$  and  $d(y)$  are calculated using Poissonian statistics and propagated into  $\bar{y}_f$  and  $\bar{y}_d$  as demonstrated by Newpower and colleagues

(2019) [4]. Plots of  $f(y)$  are multiplied by  $y$  to preserve the graphical properties of a PDF when plotted on a semi-logarithmic axis. For determination of microdosimetric parameters, a cutoff of 250 eV for the production and transport of secondary particles was used. In accordance with the recommendations of the American Association of Physicists in Medicine Task Group 268 report parameters necessary for the replicability of our Monte Carlo studies are tabulated (Table 3-1) [15].

**Table 3-1:** Summary of parameters relevant to Monte Carlo simulations conducted.

Item	Description		References
Toolkit	Geant4 10.03 P3		[11]
Cross-sections	Livermore Condensed History		[16-18]
Validation	Kyriakou <i>et al.</i> Cross Validation of Livermore with Geant4DNA.		[19-20]
Source description	microSelectron <sup>®</sup> v2 and SelectSeed <sup>®</sup>		[21-22]
Production and Tracking Cutoff of Secondary Particles	Determination of Electron Spectra	25 eV	
	Microdosimetric Calculations	250 eV	
Statistical uncertainty	10 <sup>5</sup> entries in each $f(y)$ or $d(y)$ distribution. Statistical uncertainties are determined binwise.		
Statistical methods	Binwise Poissonian uncertainties in $f(y)$ and $d(y)$ are propagated into calculated quantities		[4]

### III.III.II.III Fixed Radius Models for $f(y)$ Calculation

In order to evaluate the necessity of the full model, two models consisting of fixed radius targets were investigated. A model containing close-packed targets of the mean nucleus radius present in a histopathological sample and a model containing close-packed targets of the volume-weighted mean nucleus radius present in a histopathological sample were developed (Table 3-2). The

volume weighted mean radius refers to the radius of the average volume nucleus present in a histopathological sample – this corresponds to the mean radius of a target that a track of ionizing radiation is likely to interact with, as larger nuclei are more likely to be hit.

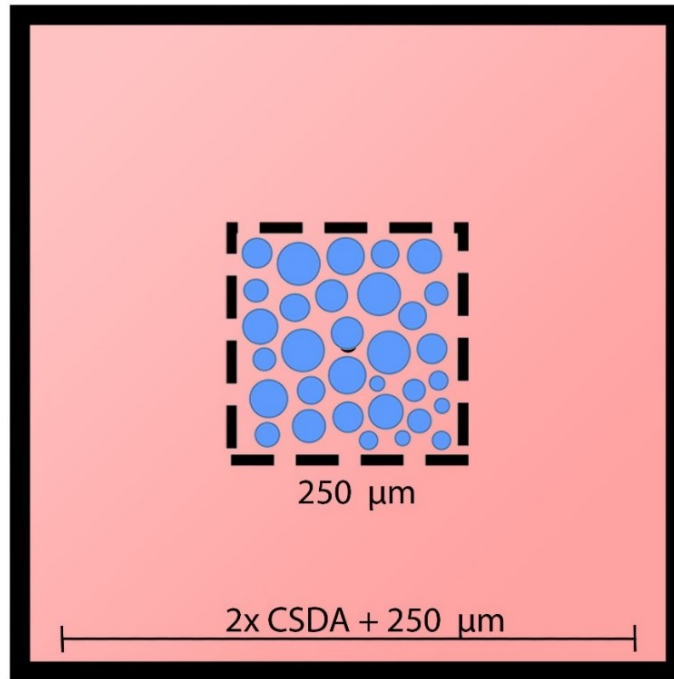


**Figure 3-2:** Two-dimensional projection of the geometry implemented in Geant4 for scoring of microdosimetric energy deposition. Shaded red region corresponds to region within which the electron spectra of interest is sampled. Region with dashed black lines contains spheres in which scoring of energy deposition events is conducted.

### III.III.II.IV Summation Method of $f(y)$ Calculation

In this study, we hypothesized that energy deposition in the fixed radius models would not well approximate energy deposition in the full model due to not considering cell spacing and variation in nucleus size. In addition, we proposed a fast method for computation of patient-specific microdosimetric distributions. A pre-calculated library of  $f(y)$  for  $^{60}\text{Co}$  and  $^{125}\text{I}$  in spheres of fixed radii from 1-14  $\mu\text{m}$  in 1  $\mu\text{m}$  increments was calculated using the same Monte Carlo approach as the previous models. In the course of the study fixed radius models were found to well approximate  $f(y)$  distributions of  $^{192}\text{Ir}$  and  $^{169}\text{Yb}$  and thus summation models were not investigated for those

sources. Patient-specific microdosimetric  $f(y)$  distributions were calculated with a weighted summation of microdosimetric distributions in spheres of fixed radius,  $r$ , yielding the function,  $f(y, r)$ :

$$f(y) = N \cdot \sum_{r=r_{\min}}^{r=r_{\max}} C_r(r) \cdot f(y, r) \quad (3 - 4)$$

Where  $C_r(r)$  is a weighting factor corresponding to the volume weighted frequency of a given cell / nucleus appearing in a histology sample:

$$C_r(r) = r^3 \cdot p_{\text{target}}(r) \quad (3 - 5)$$

Where  $p_{\text{target}}(r)$  is a patient-specific cell / nucleus radius distribution and  $N$  is simply a normalization factor given by:

$$N = \sum_{r=r_{\min}}^{r=r_{\max}} \frac{1}{C_r(r)} \quad (3 - 6)$$

Two libraries of  $f(y, r)$  were computed, one calculated in a single compartment model where fixed radius targets are close packed, and another in a two compartment model where fixed radius targets are embedded within cells of the volume weighted mean cell spacing observed in a histopathological sample (Table 3-2). Both  $\bar{y}_f$  and  $\bar{y}_d$  yielded by the summation models were compared to those given by the full model approach.

## III.IV RESULTS

### III.IV.I Generation of Three-Dimensional Tissue Models from Histological Samples

The resultant cancerous cell spacing and nucleus radii distribution is shown before and after fitting and NNLSO corrections are applied (Figure 3-3). The mean cell spacing of the cancerous regions

on the sample analyzed was 8.82  $\mu\text{m}$  with a standard deviation of 1.97  $\mu\text{m}$ , while the mean nucleus radius was 3.71  $\mu\text{m}$  with a standard deviation of 2.08  $\mu\text{m}$ . The volume weighted mean cell spacing and nucleus radius of cancerous regions in the same sample was 9.93  $\mu\text{m}$  and 5.72  $\mu\text{m}$  respectively.

**Table 3-2:** Comparison of various models in which microdosimetric parameters were determined.

Model		Cell Spacing	Nucleus Radius
Fixed Radius Models	Mean Radius	None. Nuclei close packed	Mean nucleus radius from histopathological sample
	Volume Weighted Mean Radius	None. Nuclei close packed	Volume weighted mean nucleus radius from histology sample
Variable Radius Models	Single Compartment Summation	None. Nuclei close packed	1-14 $\mu\text{m}$ (summed according to patient distribution)
	Two-Compartment Summation	Volume weighted mean cell spacing from histopathological sample	1-14 $\mu\text{m}$ (summed according to patient distribution)
	Full	Patient-specific cell spacing distribution	Patient-specific nucleus radius distribution

### III.IV.II Calculation of Microdosimetric Distributions

Lineal energy distributions for four radioisotopes in the fixed radius models and the full model are presented for the cancerous nuclei in a representative sample (Figure 3-4). The mean radius model yields values of  $\bar{y}_f$  for  $^{192}\text{Ir}$  and  $^{169}\text{Yb}$  that are within statistical uncertainties of the full model. Lineal energy  $f(y)$  distributions for  $^{60}\text{Co}$  or  $^{125}\text{I}$  are not well approximated by the fixed radius models.  $\bar{y}_f$  of the full model  $^{60}\text{Co}$  lineal energy distribution is 13% greater than either of the fixed radius models.  $\bar{y}_f$  of the full model for  $^{125}\text{I}$  is 11% less than the mean radius model and 12% greater than the volume weighted mean radius model. Unlike  $\bar{y}_f$ ,  $\bar{y}_d$  for all radioisotopes studied in the mean radius model agrees with the full model to within statistical uncertainties (Table 3-3).

Lineal energy distributions of  $^{60}\text{Co}$  generated using a summation library of  $f(y, r)$  with and without cell encapsulation is compared to the full model of a representative sample (Figure 3-5). The single compartment summation of  $\bar{y}_f$  and  $\bar{y}_d$  for  $^{60}\text{Co}$  does not agree with the full model. The  $\bar{y}_f$  and standard deviation of  $^{60}\text{Co}$  determined using the two compartment summation of  $f(y)$  is within 1.3% and 3% of the full model respectively (Figure 3-5).  $\bar{y}_f$  and  $\bar{y}_d$  determined from the two compartment summation agrees with the full model to within statistical uncertainties for both  $^{60}\text{Co}$  and  $^{125}\text{I}$  (Table 3-3). A mobile 7th generation Intel processor (i5-7300HQ) computed each summation of  $f(y)$  in less than 15 seconds using a single processor thread.

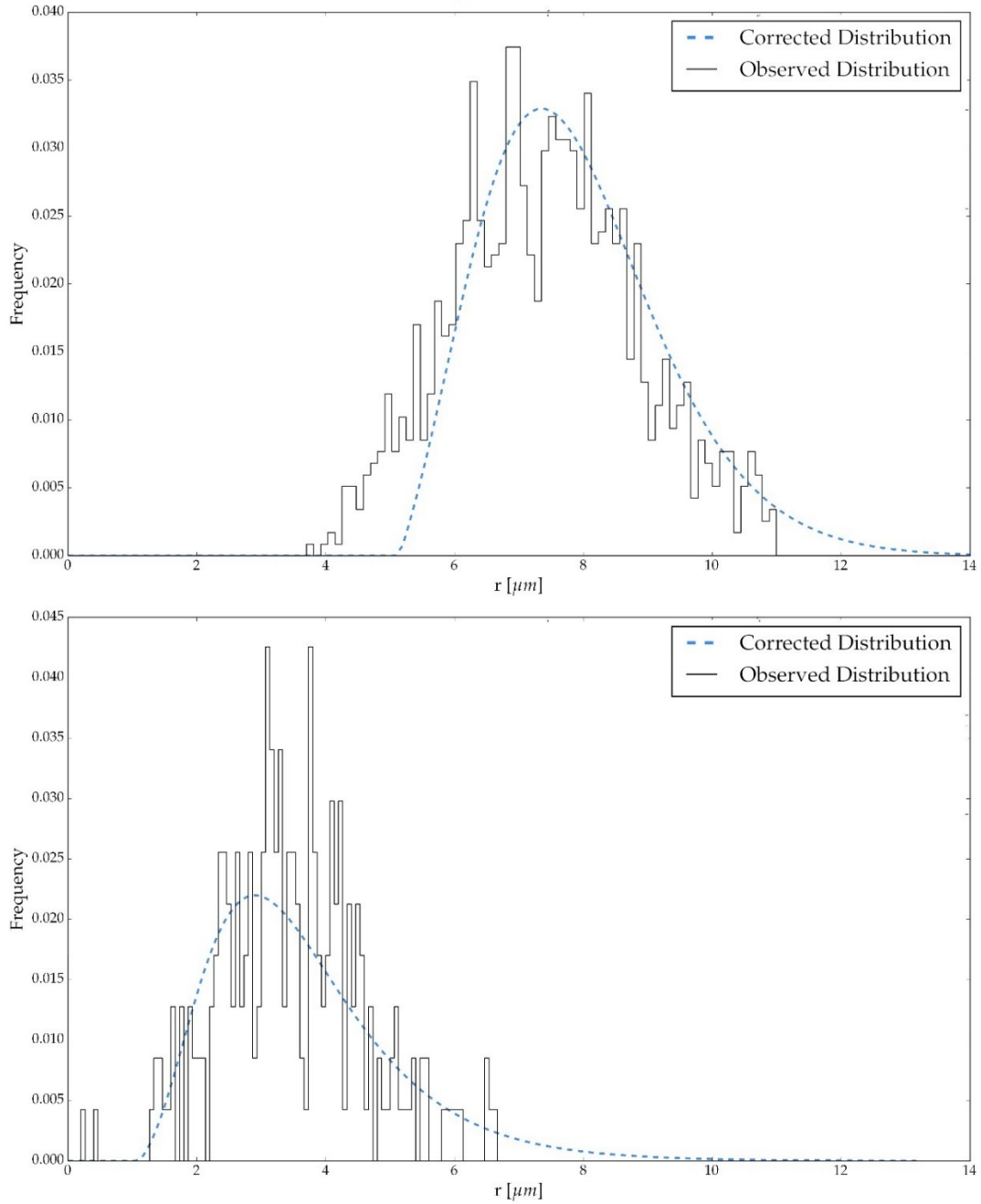
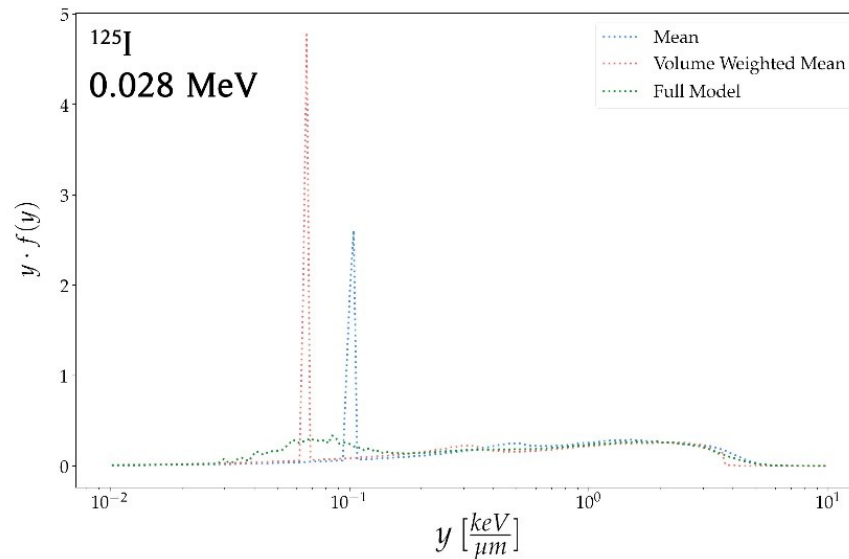
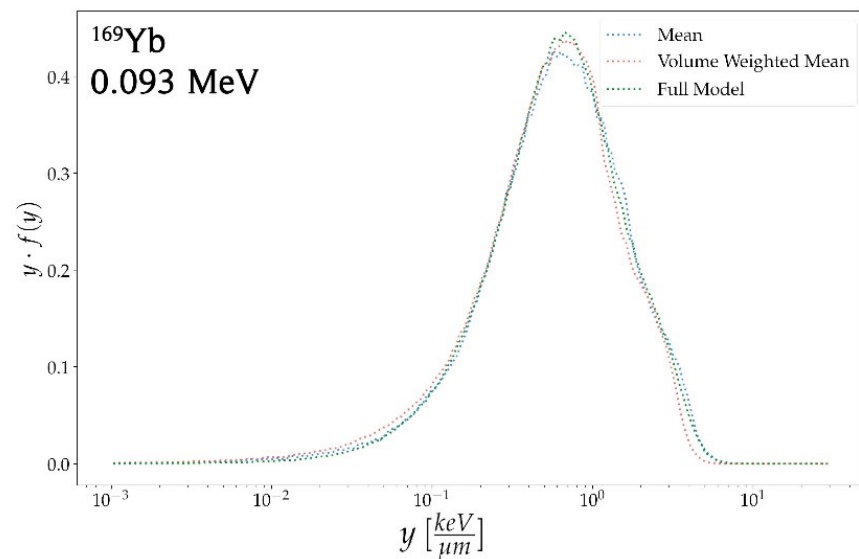
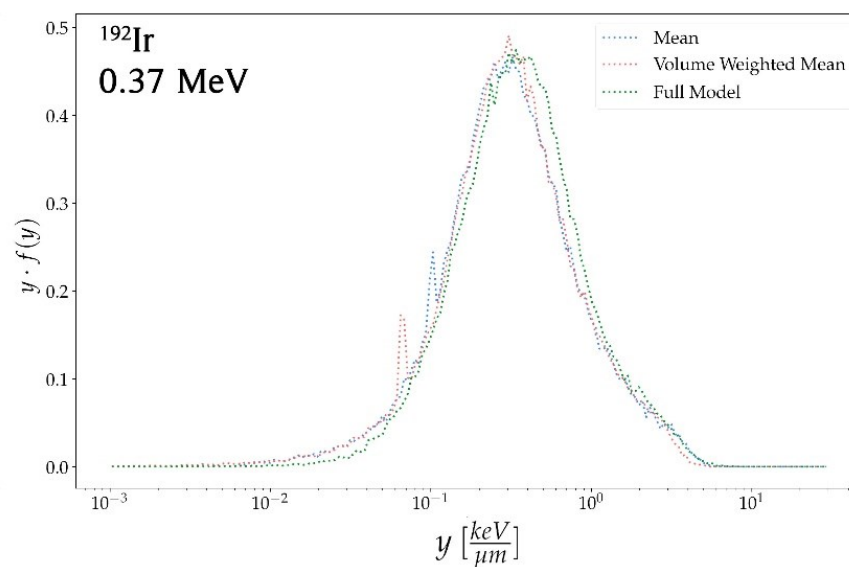
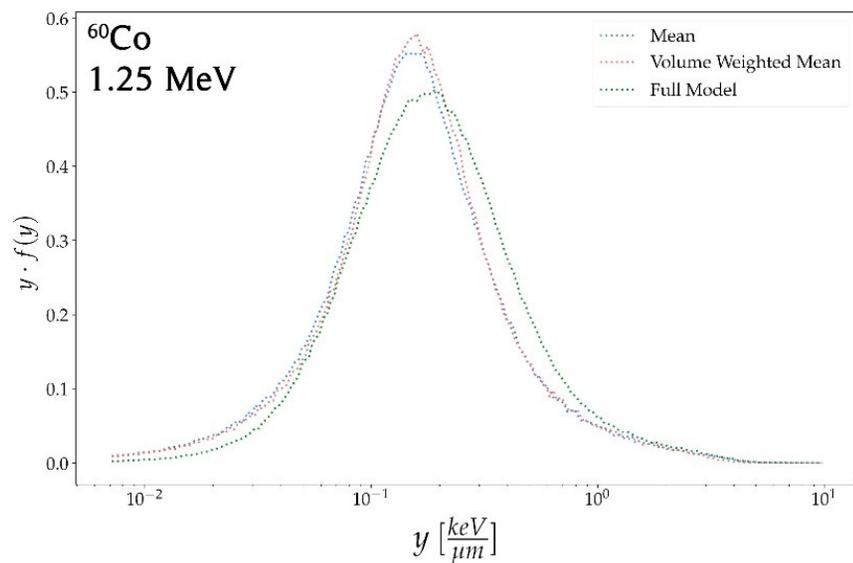


**Figure 3-3:** Observed cancerous radius distribution of representative histopathological sample and corrected size distribution after NNLSO optimization, (Top) cell spacing (Bottom) nucleus radius.



1  
 2 **Figure 3-4:**  $f(y)$  multiplied by  $y$ , are presented in the full model, mean radius model, and volume weighted mean radius model of cancerous nuclei from a single  
 3 representative sample. The inline caption represents the radioisotope investigated and mean photon energy. (Top left)  $^{60}\text{Co}$  (Top right)  $^{192}\text{Ir}$  (Bottom left)  $^{169}\text{Yb}$   
 4 (Bottom right)  $^{125}\text{I}$ .

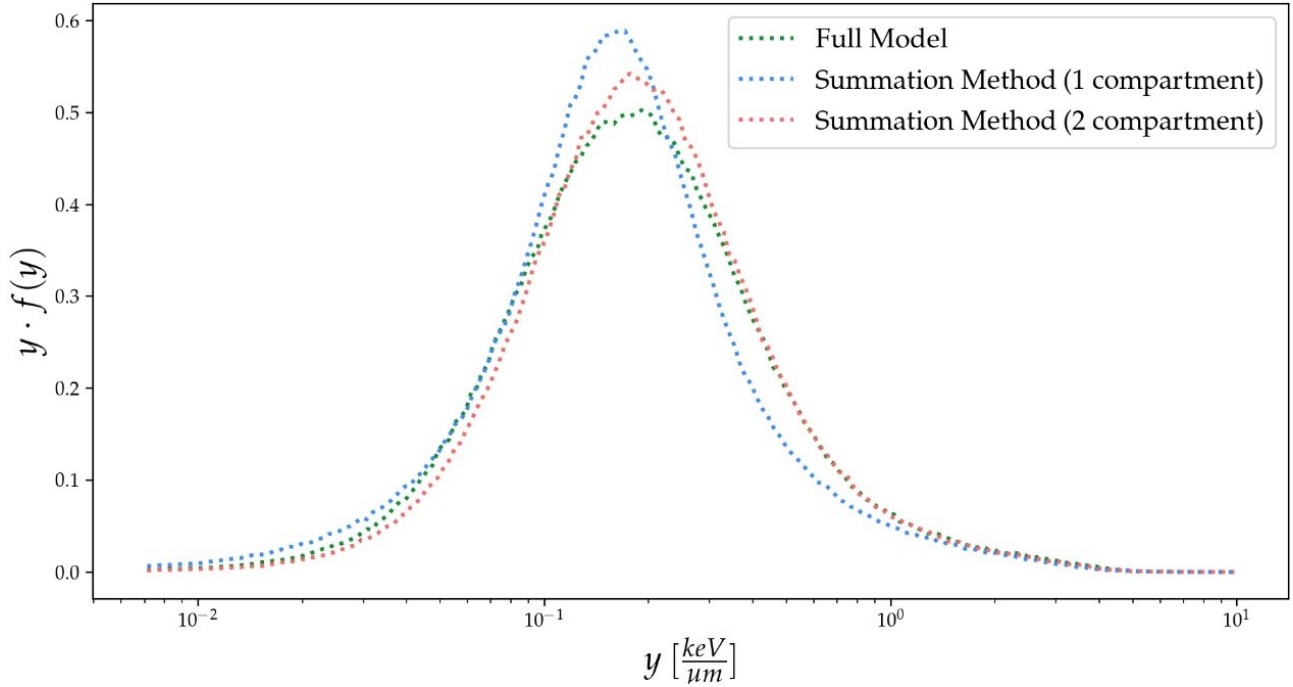


**Figure 3-5:** Comparison of patient-specific  $f(y)$  distributions of  $^{60}\text{Co}$  in a representative sample’s cancerous nuclei computed using full model (green) a single compartment summation (blue) and a two compartment summation (red).

**Table 3-3:** Comparison of  $\bar{y}_f$  and  $\bar{y}_d$  in a representative sample’s cancerous nuclei determined with several models.

Radioisotope	Mean Radius	Volume Weighted Mean Radius	Single Compartment Summation	Two Compartment Summation	Full Model
$\bar{y}_f \left[ \frac{\text{keV}}{\mu\text{m}} \right]$					
$^{60}\text{Co}$	$0.241 \pm 0.009$	$0.244 \pm 0.009$	$0.247 \pm 0.006$	$0.286 \pm 0.006$	$0.284 \pm 0.005$
$^{192}\text{Ir}$	$0.50 \pm 0.02$	$0.48 \pm 0.02$	Not Computed		$0.55 \pm 0.03$
$^{169}\text{Yb}$	$0.88 \pm 0.02$	$0.80 \pm 0.01$	Not Computed		$0.88 \pm 0.01$
$^{125}\text{I}$	$0.80 \pm 0.01$	$1.00 \pm 0.01$	$0.84 \pm 0.03$	$0.85 \pm 0.05$	$0.90 \pm 0.01$
$\bar{y}_d \left[ \frac{\text{keV}}{\mu\text{m}} \right]$					
$^{60}\text{Co}$	$0.74 \pm 0.05$	$0.67 \pm 0.05$	$0.69 \pm 0.03$	$0.74 \pm 0.03$	$0.77 \pm 0.04$
$^{192}\text{Ir}$	$1.23 \pm 0.09$	$1.10 \pm 0.07$	Not Computed		$1.24 \pm 0.08$
$^{169}\text{Yb}$	$1.68 \pm 0.10$	$1.47 \pm 0.03$	Not Computed		$1.65 \pm 0.03$
$^{125}\text{I}$	$2.18 \pm 0.05$	$1.87 \pm 0.03$	$1.96 \pm 0.06$	$2.1 \pm 0.2$	$2.12 \pm 0.03$

## III.V DISCUSSION

### III.V.I Generation of Three-Dimensional Tissue Models from Histological Samples

This study restricts itself to the investigation of microdosimetric distributions determined in volumes whose sizes are derived from a single histopathological sample. The accuracy of approximate methods for the fast calculation of patient-specific microdosimetric distributions can be evaluated by comparison to a full model developed from a single sample. Remaining questions regarding patient-specific microdosimetry exist for which study of tissue models developed from histopathological data gathered from multiple patients will be necessary. A systematic study of the effect of packing density of three-dimensional models developed on the resultant microdosimetric distribution has not yet been conducted. Furthermore, the inter-patient variability in microdosimetric distributions computed from patient-specific data is not yet known.

### III.V.II Fixed Radius Models for $f(y)$ Calculation

Patient-specific microdosimetric distributions are microdosimetric functions determined in cell and nucleus volumes whose sizes are obtained from histopathological samples [23,10]. Calculation of such distributions require computational resources on the order of 1 core-year and thus are not currently viable for use in a clinical environment. Approximate methods to obtain those quantities quickly and with minimal computational resources were investigated including fixed radius models. However, the fixed radius models did not provide a close approximation of the full model  $f(y)$  for  $^{60}\text{Co}$  and  $^{125}\text{I}$ , which are the radionuclides with the greatest and least mean photon energies studied respectively. Our results indicate that, in addition to the secondary electron spectra of the radionuclide investigated, target size, and target spacing are relevant parameters for the computation of microdosimetric quantities. In the fixed radius models, in addition to having fixed

radius nuclei, the spacing between the nuclei is also disturbed leading to the approximation of  $f(y)$  to be inaccurate for  $^{60}\text{Co}$ . The cell spacing is not relevant for  $^{125}\text{I}$  as few electrons generated traverse more than one target, since their average electron energy is much lower and thus have shorter ranges. Instead, electrons in the  $^{125}\text{I}$  spectrum deposit all their energy in a single target, generating peaks in  $f(y)$ . The peaks in the  $f(y)$  spectrum of  $^{125}\text{I}$  are entirely characteristic of the electron energy and target size. A fixed radius model cannot approximate  $f(y)$  of the full model when the range of electrons generated by a source are either less than or much larger than the target size.

A strong  $f(y)$  dependence on cell spacing for higher energy sources and strong dependence on nucleus size for lower energy sources explains the disagreement observed in Figure 3-4. It is worth noting that the effect of cell / target spacing on microdosimetric distributions has not been studied systematically elsewhere to our knowledge. The relative agreement of the fixed radius models with the full model for  $f(y)$  of  $^{192}\text{Ir}$  and  $^{169}\text{Yb}$  can be explained by understanding that the secondary electrons set in motion by these radioisotopes have such an energy that they tend to traverse entire nucleus targets, while not having an adequate energy to traverse more than one such target, yielding a weaker dependence on both target size and cell spacing. The mean nucleus radius model is an appropriate approximation for  $f(y)$  and  $\bar{y}_d$  of  $^{192}\text{Ir}$  and  $^{169}\text{Yb}$ .

The mean radius model yields a  $\bar{y}_d$  value closer to the full model than the volume weighted model (Table 3-3).  $\bar{y}_d$  of the mean radius model agrees with the full model within statistical uncertainties for all sources studied. These results suggest that if one intends to approximate a patient-specific  $\bar{y}_d$ , but not a complete  $f(y)$  distribution, in nucleus sized volumes, use of the mean nucleus radius may be an appropriate surrogate.

### III.V.III Summation Method of $f(y)$ Calculation

Two summation method approximations of patient-specific  $f(y)$  distributions are presented in Figure 3-5. As noted previously,  $f(y)$  distributions of  $^{60}\text{Co}$  show a strong dependence on cell spacing, it is then not surprising that the two compartment summation method yields an  $f(y)$  distribution of  $^{60}\text{Co}$  which is closest to the full model of all of the approximations studied (Figure 3-5). As shown in Table 3-3,  $\bar{y}_f$  and  $\bar{y}_d$  yielded from the two-compartment summation method agrees with the full model within statistical uncertainties for both  $^{60}\text{Co}$  and  $^{125}\text{I}$ . The summation method approximation of  $^{125}\text{I}$  should improve in agreement with the full model if additional terms were added to the summation, as  $f(y)$  is strongly dependent on target size. The summation method was not applied to  $^{192}\text{Ir}$  and  $^{169}\text{Yb}$  as fixed radius models yielded an appropriate approximation of  $f(y)$ .

The use of such a two-compartment summation can allow for the computation of patient-specific microdosimetric distributions of  $f(y)$  and  $d(y)$  in seconds with only the computing power of a personal computer. Formerly calculation of such patient-specific distributions would have taken on the order of 10,000 core hours on a supercomputing cluster. This can make patient-specific microdosimetry clinically feasible and available for those without extensive computational resources. The formalism for summation approximation of  $f(y)$  is also trivially extendable to  $f_1(z)$  or  $f(z, D)$  if knowledge of spread in specific energy rather than lineal energy is desired.

### III.V.IV Applications of Patient and Tissue-Specific Microdosimetry

Microdosimetric quantities can be used as inputs to radiobiological models which characterize RBE [24]. Knowledge of the RBE of radiation qualities including low energy photons, light and heavy ions compared to MeV photon irradiations allows novel therapies to be planned using the

extensive quantity of outcome data which has been accumulated from decades of treatment with MeV photons. While not currently used clinically, an understanding of RBE may be important in the planning of treatments with low and intermediate energy photon emitting brachytherapy sources such as  $^{125}\text{I}$ ,  $^{169}\text{Yb}$ ,  $^{103}\text{Pd}$ , and low energy x-ray sources for which an enhancement in RBE has been observed in vitro [25-33]. The microdosimetric kinetic model (MKM) which describes the time-varying processes of cellular damage repair and can take inputs from observable microdosimetric quantities may be a viable model for the determination of RBE of low energy photon emitting brachytherapy sources [34]. A formulation of the MKM which requires  $f(y)$  in nucleus sized volumes has been developed by Kase *et al.* (2006) [24]. The results presented here further support the understanding that consideration of variable radius models is necessary to accurately characterize anticipated microdosimetric distributions in vivo. Patient-specific microdosimetric distributions could yield a patient-specific RBE if incorporated with an appropriate radiobiological model. Clinical adoption of RBE to plan novel brachytherapy treatments may yield greater prognostic ability and allow for modifications to the dose prescription according to the anticipated biological effect, which may improve treatment outcomes.

### III.VI CONCLUSIONS

In this study, microdosimetric distributions determined in models derived from patient-specific information were determined for the first time. The use of a two-compartment summation method allows for the computation of patient-specific microdosimetric distributions of  $f(y)$  and  $d(y)$  in seconds with only the computing power of a typical personal computer.

Patient-specific microdosimetry has applications in basic science and in the clinic. With appropriate biological inputs the microdosimetric distributions computed using these methods can yield a patient-specific RBE as part of a multiscale treatment planning approach. A greater

understanding of patient-specific dose response may improve prognostic ability or allow for dose modification which can improve treatment outcomes.

## References

- [1] Rossi H.H, Zaider M. *Microdosimetry and Its Applications*. Berlin, Germany, Springer-Verlag, 1996.
- [2] Lindborg L, Waker A. *Microdosimetry: Experimental Methods and Applications*. Boca Raton, USA, CRC Press, 2017.
- [3] Booz J, Braby L, Coyne J, et al. *Microdosimetry (ICRU Report 36)*. J. ICRU. 1983;19(1).
- [4] Newpower M, Patel D, Bronk L, et al. Using the Proton Energy Spectrum and Microdosimetry to Model Proton Relative Biological Effectiveness. *Int. J. Radiat. Oncol. Biol. Phys.* 2019;104(2):316-324.
- [5] Oliver P.A.K, Thomson R.M. Investigating energy deposition within cell populations using Monte Carlo simulations. *Phys. Med. Biol.* 2018;63(15).
- [6] Villegas F, Tilly N, Ahnesjö A. Microdosimetric spread for cell-sized targets exposed to Co-60, Ir-192 and I-125 sources. *Radiat. Prot. Dosim.* 2015;166(1-4):365-368.
- [7] Mori R, Matsuya Y, Yoshii Y, et al. Estimation of the radiation-induced DNA double-strand breaks number by considering cell cycle and absorbed dose per cell nucleus. *Radiat. Res.* 2018;59(3):253-260.
- [8] Broët P, Dalmaso C, Tan E.H, et al. Genomic profiles specific to patient ethnicity in lung adenocarcinoma. *Clin. Cancer. Res.* 2011;17(11):3542-3550.
- [9] Enger SA, Ahnesjö A, Verhaegen F, et al. Dose to tissue medium or water cavities as surrogate for the dose to cell nuclei at brachytherapy photon energies. *Phys. Med. Biol.* 2012;57:4489-4500.
- [10] DeCunha J, Villegas F, Vallières F, et al. Development of Tissue Specific 3D Models for Investigation of Energy Deposition Properties of Ionizing Radiation. Under review, 2020.
- [11] Allison J, Amako K, Apostolakis J, et al. Recent developments in Geant4. *Nucl. Instr. Meth. Phys. Res.* 2016;835:186-225.
- [12] Tuli JK. *Evaluated nuclear structure data file, a manual for preparation of data sets*. 1987. (Berkeley, CA: Lawrence Berkeley National Laboratory).
- [13] Loken C, Grunger D, Groer L, et al. SciNet: lessons learned from building a power-efficient top-20 system and data centre. *J. Phys. Conf. Ser.* 2010;256:1-35.
- [14] Berger, M.J., Coursey, J.S., Zucker, M.A., et al. *ESTAR, PSTAR, and ASTAR: Computer Programs for Calculating Stopping-Power and Range Tables for Electrons, Protons, and Helium Ions (version 1.2.3)*. [Online] (2005), Available: <http://physics.nist.gov/Star> [Accessed: 2019, July 20]. National Institute of Standards and Technology, Gaithersburg, MD.

- [15] Sechopoulos I, Rogers D.W.O, Bazalova-Carter M, *et al.* RECORDS: improved Reporting of monte Carlo Radiation transport Studies: Report of the AAPM Research Committee Task Group 268. *Med. Phys.* 2018;48(1):e1-e5.
- [16] D. E. Cullen, J. H. Hubbell, and L. Kissel. EPDL97: The evaluated photon data library, 97 Version, Report No. UCRL-LR-50400-V6-R5. Lawrence Livermore National Laboratory, Livermore, 1997.
- [17] S. T. Perkins, D. Cullen, M. Chen, *et al.* Tables and graphs of atomic subshell and relaxation data derived from the LLNL evaluated atomic data library (EADL), Z  $\frac{1}{4}$  1-100, Report No. UCRL50400-V30, Lawrence Livermore National Laboratory, Livermore, 1991.
- [18] S. Perkins, D. Cullen, and S. Seltzer. Tables and graphs of electroninteraction cross-sections from 10 eV to 100 GeV derived from the LLNL evaluated electron data library (EEDL), Z  $\frac{1}{4}$  1-100, Report No. UCRL50400-V31, Lawrence Livermore National Laboratory, Livermore, 1991.
- [19] Kyriakou I, Ivanchenko V, Sakata D, *et al.* Influence of track structure and condensed history physics models of Geant4 to nanoscale electron transport in liquid water. *Phys. Med.* 2019;58:149-154.
- [20] Kyriakou I, Emfietzoglou, Ivanchenko V, *et al.* Microdosimetry of electrons in liquid water using the low-energy models of Geant4. *Jour. Appl. Phys.* 2017;122:024303-1-024303-15.
- [21] Daskalov GM, Löffler E, Williamson JF. Monte Carlo-aided dosimetry of a new high dose-rate brachytherapy source. *Med Phys* 1998;25:2200-2208.
- [22] Karaikos P, Papagiannis P, Sakelliou L, *et al.* Monte Carlo dosimetry of the selectSeed 125I interstitial brachytherapy seed. *Med Phys* 2001; 28:1753-1760.
- [23] Poole C.M, Ahnesjö A, Enger S.A. Determination of subcellular compartment sizes for estimating dose variations in radiotherapy. *Radiat. Prot. Dosim.* 2015;166(1-4):361-364.
- [24] Kase Y, Kanai T, Matsumoto Y, *et al.* Microdosimetric measurements and estimation of human cell survival for heavy-ion beams. *Radiat. Res.* 2006;166(4):629-638.
- [25] Nikjoo H, Lindborg L. RBE of low energy electrons and photons. *Phys. Med. Biol.* 2010;55:R65-R-109.
- [26] McDonald JC, Ma I, Zeitz L. Microdosimetric properties of encapsulated 125I and other photon sources. *Radiat Res* 1979.
- [27] Wu CS, Zaider M. A calculation of the relative biological effectiveness of 125I and 103Pd brachytherapy sources using the concept of proximity function. *Med Phys* 1998;25:2186-2189.
- [28] Wu CS, Kliuga P, Zaider M, *et al.* Microdosimetric evaluation of relative biological effectiveness for 103Pd, 125I, 241Am, and 192Ir brachytherapy sources. *Int J Radiat Oncol Biol Phys* 1996;36:689-697. 77:221-232.
- [29] Reniers B, Vynckier S, Verhaegen F. Theoretical analysis of microdosimetric spectra and cluster formation for 103Pd and 125I emitters. *Phys Med Biol* 2004;49:3781-3795.

- [30] Wu CS, Chen J. Calculated microdosimetric characteristics of <sup>125</sup>I and <sup>103</sup>Pd brachytherapy seeds at different depths in water. *Radiat Prot Dosimetry* 2006;122:506-508.
- [31] Hill MA. The variation in biological effectiveness of low energy x-rays and gamma rays with energy. *Radiat Prot Dosimetry* 2008;112:471-481.
- [32] Brenner DJ, Leu CS, Beatty JF, et al. Clinical relative biological effectiveness of low-energy x-rays emitted by miniature x-ray devices. *Phys Med Biol* 1999;44:323-333.
- [33] Famulari G, Pater P, Enger S.A. Microdosimetric Evaluation of Current and Alternative Brachytherapy Sources – A Geant4-DNA Simulation Study. *Int. J. Radiat. Oncol. Biol. Phys.* 2017;100(1):270-277.
- [34] Hawkins R.B. A microdosimetric-kinetic model of cell death from exposure to ionizing radiation of any LET, with experimental and clinical applications. *Int. J. Radiat. Biol.* 1996;69(6):739-755.

## Chapter IV: Further Investigations

### IV.I Target Spacing Dependence of Microdosimetric Distributions

When attempting to approximate  $f(y)$  and  $d(y)$  distributions of nuclei under irradiation by  $^{60}\text{Co}$ , it was observed that the spacing between adjacent nucleus targets affected the microdosimetric distributions calculated (Figure 3-5). To the best of our knowledge, a dependence on target spacing of  $f(y)$  distributions has never before been observed. This is likely because existing methods in experimental microdosimetry use detectors which measure energy depositions in a single target and thus have no concept of target spacing [1]. Methods which have been employed in computational microdosimetry previously, either make use of a grid of cubic or spherical targets without spacing or make use of track sampling algorithms which involve superimposing volumes on top of ionizing radiation track structure data [2-4]. Spacing between targets is neglected in both simple grid based models and with track sampling algorithms.

As the observed dependence of microdosimetric distributions on target spacing has not been previously reported, further investigations are warranted, both to verify this result and better develop a conceptual understanding of why target spacing affects microdosimetric distributions. An investigation of the dependence of  $f(y)$  on target spacing could be conducted by gathering track structure information of a radiation source using MC methods. The track structure information could then be superimposed on a grid of spheres spaced apart by a given distance. The superposition of track structure information on models is suggested to improve the computational efficiency of the investigation, as tracks can be re-used and superimposed on models of many different target spacings. The variation of  $f(y)$  as a function of target spacing can then be determined and hypotheses regarding the causes of such variation developed.

If target spacing is confirmed to impact  $f(y)$ , then target spacing in some way must be biasing the scoring ratio of various track segments. A model in which the beginning, middle, and end of track segments are signified by the colours green, yellow, and blue is introduced in Figure 4-1. In the limit that there is no target spacing, the 2D model shows that on average each segment of the track is scored an equivalent amount. Similarly, in the limit that the spacing between targets is greater than the range of the track each track segment is scored an equivalent amount.

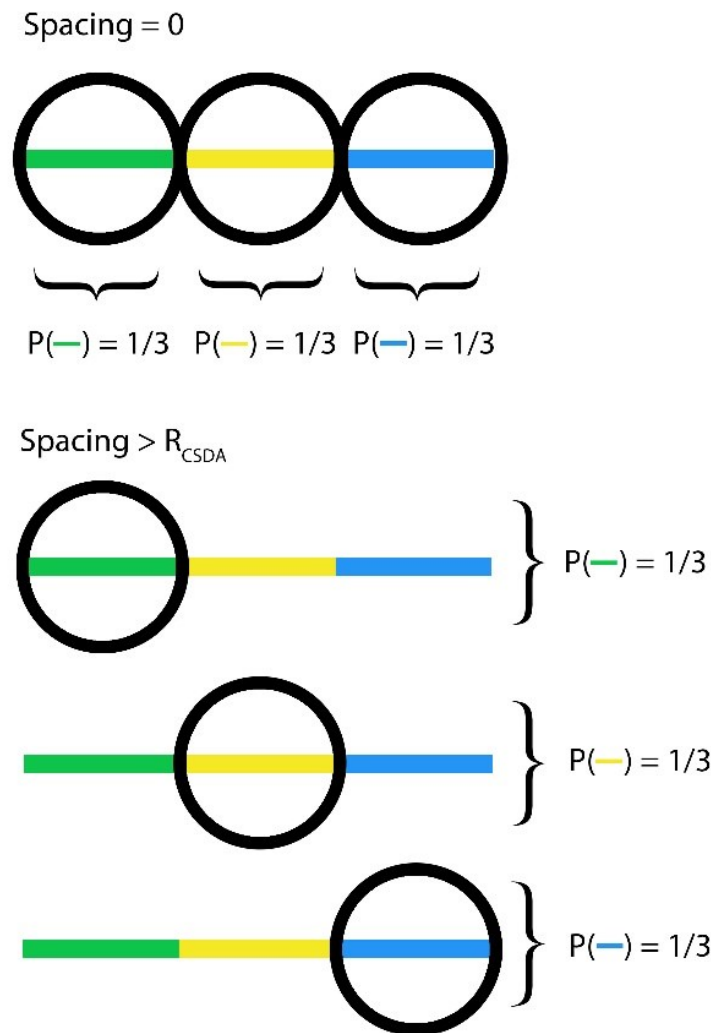
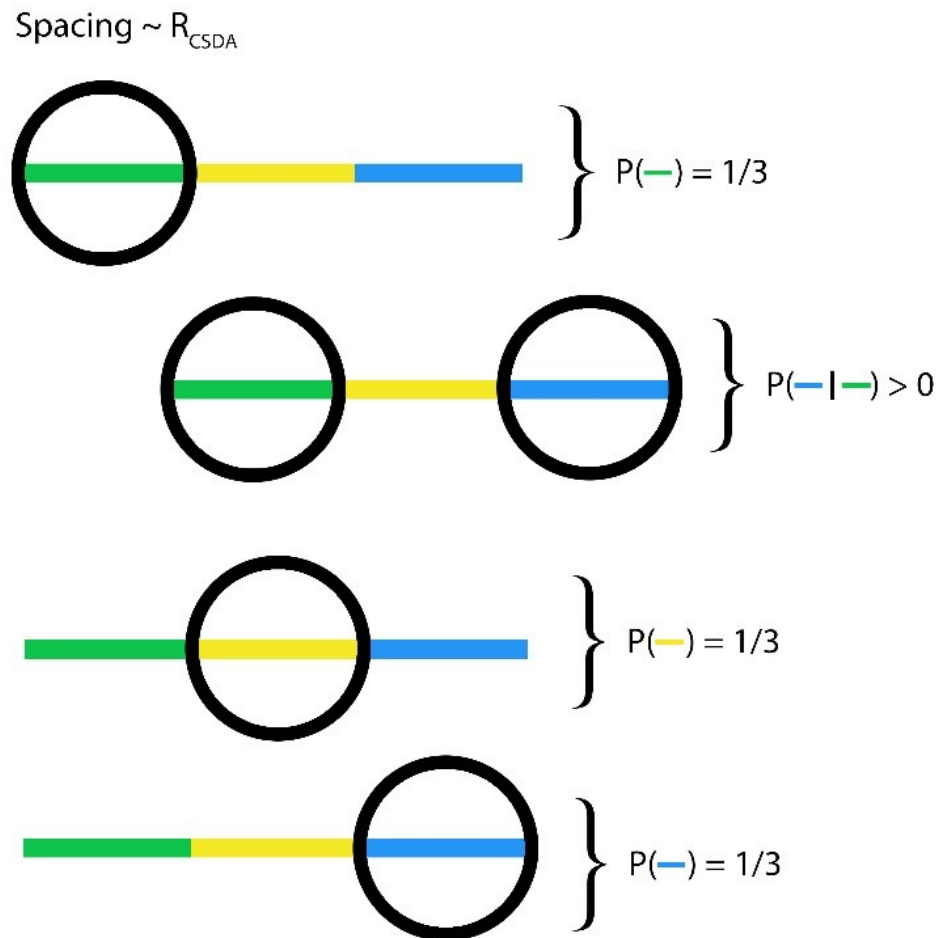


**Figure 4-1:** 2D model of the probability of various track segments being scored as a function of target spacing. The beginning, middle, and end of the track are signified by the colours green, yellow, and blue respectively. (Top) target spacing = 0 (Bottom) target spacing greater than range of the track.

However, in the limit that the target spacing is less than or comparable to the range of the track, the model predicts that a bias towards scoring of track ends may occur as shown in Figure 4-2. The total probability of scoring of the track end is equal to the summation of the track end being scored on its own, and the conditional probability of the track end being scored after the track beginning has been scored.



$$P_{\text{TOT}}(-) = P(-) + P(- | -) > 1/3$$

**Figure 4-2:** 2D model of the probability of various track segments being scored when the target spacing is approximately the range of the track. The beginning, middle, and end of the track are signified by the colours green, yellow, and blue respectively.

## IV.II Inter-patient Variation in Radiosensitivity

This work further emphasizes the knowledge that microdosimetric parameters are dependent on target size and that fixed and variable radius models may not yield equivalent microdosimetric results. Given that living tissues contain a multitude of cells and nuclei of various sizes, variable radius models should more accurately characterize anticipated microdosimetric distributions *in vivo* than existing methods. The patient-specific microdosimetric distributions developed from variable radius models presented in this thesis have the potential to be paired with radiobiological models in order to make patient-specific predictions of RBE. We expect variation in  $f(y)$  and in  $d(y)$  observed between fixed and variable radius models should yield differing predictions of RBE when microdosimetric distributions are propagated through a radiobiological model. The methods through which patient-specific microdosimetric distributions may be paired with radiobiological models are numerous and two potential such methods will be described here.

A method by Kase *et al.* has been proposed to use the MKM to determine  $\alpha$  and  $\beta$  which characterizes RBE for a given cell line from a combination of biological and microdosimetric data [5]. The method by Kase makes no distinction between  $y$  in nanoscopic domains and in the entire nucleus, which relies on the assumption that  $f(y)$  distributions are independent of target size. The method proposed by Kase can be modified to make predictions of RBE given two sets of  $f(y)$ , one determined in nucleus size targets and another in nanoscopic domains. Patient-specific  $f(y)$  distributions may then be readily integrated into the MKM to make patient-specific predictions of RBE.

Similarly, knowledge of nucleus size distributions will yield knowledge which may be integrated into the LEM. While, most recent versions of the LEM consider local energy depositions in domains of the nucleus, the nucleus size is still a relevant parameter when making LEM

calculations. Typically, fixed nucleus radii between 5-10  $\mu m$  are assumed when determining energy depositions for the LEM. The cluster index should depend on nucleus size, as the cluster index is calculated by the ratio of clustered and unclustered damage observed across the entire nucleus. As greater deviations of lineal energy from the mean are observed in smaller targets, greater stochastic variation in cluster index is expected to be observed in smaller nuclei. Additionally, it is not yet known if models which include cell spacing and variable nucleus sizes will effect  $f(y)$  determined in nucleus domains themselves. Both the dependence of cluster index on nucleus size, and potential dependence of  $f(y)$  in nucleus domains on cell spacing and nucleus size suggest that the tissue-specific models developed in this work may yield differing predictions of RBE than current adaptations of the LEM.

It remains to be seen if  $f(y)$  determined in nucleus sized targets of various sizes arranged in a non-geometric fashion yields a meaningfully different RBE when propagated through a radiobiological model compared to conventional methods. Patient-specific microdosimetry will only prove valuable if inter-patient variation in microdosimetric distributions is significant enough to confer differing radiobiological effects. Further investigations remain to be done to determine the specific radiation qualities and cancer pathologies for which patient-specific microdosimetric distributions will deviate the greatest from microdosimetric distributions determined in conventional fixed radius models. Determination of a patient-specific RBE will allow for patient-specific modelling of dose response which should enhance prognostic abilities or allow for dose modifications in RT.

#### **IV.III Cell Cycle Dependence of Radiosensitivity to DNA DSB Induction**

Tissue-specific models have potential applications in basic science where conventional microdosimetric methods in simple geometries have been used to explain variability in DNA DSB induction *in vitro* [6]. Currently a combination of microdosimetric information and cell cycle

information is needed in order to characterize inter-cell variability in DNA DSB induction. A method proposed by Mori *et al.* involves the determination of specific energy distributions,  $f(z, D)$ , in a grid of cubes with equivalent volume to a 10  $\mu\text{m}$  diameter sphere. The yield of DSBs induced per cell is assumed be linear with dose and is given the value  $30 \frac{\text{DSB}}{\text{Gy}\cdot\text{Cell}}$ . The yield of DSBs predicted by microdosimetry is then weighted by a cell cycle model that accounts for the relative amount of DNA present in the nucleus and applies a correction for background DSB formation as a function of cell cycle. If microdosimetry were conducted in a more accurate model of the cell line which included variability in cell spacing and nucleus size, a cell cycle model may not be necessary to characterize DSB formation. If true, this would confirm the hypothesis that cell cycle variation in DNA DSB induction is a function of nucleus volume alone and intrinsic radiosensitivity to DNA DSB formation does not vary throughout the cell cycle.

#### **IV.IV Calculation of S-values in Radiopharmaceutical Therapy**

RPT involves the intravenous injection of a radionuclide attached to a targeting molecule which causes the radiopharmaceutical compound to become preferentially concentrated in cancerous tissues. Various methods for conducting dosimetry in RPT have been proposed, though the most widespread is known as the medical internal radiation dose (MIRD) method. [7]. A quantity necessary to perform dosimetry using the MIRD formalism is the absorbed dose per unit activity, also known as the S-value [8]. If the accumulated activity is known in a region the S-value allows one to determine the mean absorbed dose in a volume of interest. S-values can convert from an accumulated activity to a mean organ dose, or to dose in a specific microscopic volume such as the cell or cell nucleus. S-values are typically calculated using either analytic or MC methods [8-9]. Often, spherical volumes of fixed size are used for the calculation of cellular or nucleus S-values. In order to more accurately characterize S-values of radiopharmaceuticals cell and nucleus

models determined using confocal microscopy have been used to determine the geometry of MC simulations [10]. Accurate knowledge of S-values and microdosimetric information will be particularly valuable for radiopharmaceuticals which rely on the emission of Meitner-Auger electrons, beta, or alpha particles for tumour ablation. Extreme microscopic variability in energy deposition between biological volumes of interest occurs because of the low number of tracks which will deposit energy in any given target, owing to the short track lengths and high LET of Meitner-Auger electrons and alpha particles. Knowledge of the size and spacing between a population of cells should influence a quantity known as the cross S-value, the mean absorbed dose deposited in a volume from a radionuclide which decayed in another nearby volume. As existing calculations of cross S-values are frequently computed in single sized volumes placed in a simple grid, the models described in this thesis should allow for a more accurate computation of cross S-values than existing methods.

## References

- [1] Lindborg L, Waker A. Microdosimetry: Experimental Methods and Applications. Boca Raton, USA, CRC Press, 2017.
- [2] Villegas F, Tilly N, Ahnesjö A. Microdosimetric spread for cell-sized targets exposed to Co-60, Ir-192 and I-125 sources. *Radit. Prot. Dosim.* 2015;166(1-4):365-368.
- [3] Villegas F, Tilly N, Ahnesjö A. Target Size Variation in Microdosimetric Distributions and its Impact on the Linear-Quadratic Parameterization of Cell Survival. *Radiat. Res.* 2018;190(5):504-512.
- [4] Famulari G, Pater P, Enger S.A. Microdosimetric Evaluation of Current and Alternative Brachytherapy Sources – A Geant4-DNA Simulation Study. *Int. J. Radiat. Oncol. Biol. Phys.* 2017;100(1):270-277.
- [5] Kase Y, Kanai T, Matsumoto Y, et al. Microdosimetric measurements and estimation of human cell survival for heavy-ion beams. *Radiat. Res.* 2006;166(4):629-638.
- [6] Mori R, Matsuya Y, Yoshii Y, et al. Estimation of the radiation-induced DNA double-strand breaks number by considering cell cycle and absorbed dose per cell nucleus. *Radiat. Res.* 2018;59(3):253-260.

- [7] Bolch W.E, Eckerman K.F, Sgouros G, *et al.* MIRD Pamphlet No. 21: A Generalized Schema for Radiopharmaceutical Dosimetry—Standardization of Nomenclature. *J. Nucl. Med.* 2009;50:477-484.
- [8] Goddu S.M, Howell R.W, Dandamudi V.R. Cellular Dosimetry: Absorbed Fractions for Monoenergetic Electron and Alpha Particle Sources and S-values for Radionuclides Uniformly Distributed in Different Cell Compartments. *J. Nucl. Med.* 1994;35:303-316.
- [9] Bousis C, Emfietzoglou D, Hadjidoukas P, *et al.* Monte Carlo single-cell dosimetry of Auger-electron emitting radionuclides. *Phys. Med. Biol.* 2010; 55(9): 2555-2572.
- [10] Tamborino G, Saint-Hubert M.D, Struelens L, *et al.* Cellular dosimetry of [<sup>177</sup>Lu]Lu-DOTA-[Tyr<sup>3</sup>]octreotate radionuclide therapy: the impact of modeling assumptions on the correlation with in vitro cytotoxicity. *Eur. J. Nucl. Med. Mol. I. Phys.* 2020;7(8).

## Chapter V: Conclusions

This thesis describes a series of studies which have the aim of developing methods to allow for patient-specific microdosimetry. An automated algorithm for extraction of cell spacing and nucleus radius information is developed which is suitable for use with hematoxylin and eosin stained histopathological samples comparable to those extracted during clinical practice. The methods developed are capable of distinguishing between non-tumoral and cancerous cell spacing and nucleus radius distributions determined from different regions of the same sample. Three-dimensional digital tissue models with equivalent cell spacing, nucleus radius, and packing density as cancerous tissues are developed and have applications in microdosimetry and basic science.

Patient-specific microdosimetric distributions are determined in tissue models. A method which allows for the computation of patient-specific microdosimetric distributions in seconds using a desktop computer is developed to allow for further clinical and research adoption of patient-specific microdosimetric data. Microdosimetric distributions in patient and tissue-specific models can be used to predict RBE, to compute S-values for theragnostic therapies, and to better quantify the cell cycle dependence of DNA damage induction from ionizing radiation.

Further work remains to be done to pair the microdosimetric results of this thesis with radiobiological models to calculate the anticipated inter-patient radiobiological effects of cell and nucleus size variation. We observed a dependence of microdosimetric distributions on the spacing between adjacent targets. Additional work should be performed to verify and study the dependence of target spacing on microdosimetric distributions.